

3

Ice Crystal Complexity and Link to the Cirrus Cloud Radiative Effect

Emma Järvinen¹, Bastiaan van Dierenhoven², Nathan Magee³, Steven Neshyba⁴, Martin Schnaiter¹, Guanglang Xu¹, Olivier Jourdan⁵, David Delene⁶, Fritz Waitz¹, Simone Lolli⁷, and Seiji Kato⁸

ABSTRACT

The aim of this chapter is to present emerging information on ice crystal morphology in the nano- and microscale from various sources, and explore its impact on ice crystal's single-scattering properties and ultimately on cirrus cloud radiative effect. Increasing amount of observations in the last decade have shown that cirrus ice crystals invariably contain some degree of facet roughness, hollowness, or other morphological complexities that make the crystal shape deviate from that of a pristine hexagonal shape. These morphological complexities are found to be present in a wide variety of environmental conditions. A set of physical and statistical complexity parameters is used to quantify ice crystal complexity depending on the application. Although laboratory studies have shown that complexity parameters tend to increase with increasing crystal growth rate, observations in natural cirrus indicate that complexity parameters only weakly vary at cirrus temperatures below 230 K. Morphological complexities affect the optical properties of ice crystals. Implementing the optical properties of complex ice crystals in climate models has shown that the radiative effect of crystal complexity is a cooling of 1–2 Wm⁻² globally. Due to the prevalence of ice crystal morphological complexities and their influence on cirrus radiative properties, the radiative effect of crystal complexity should be taken into account in future climate models. However, work is still needed to transfer the increasing knowledge of the physical nature of ice crystal complexity into optical particle models and eventually into parameterizations used in models.

¹*Institute of Meteorology and Climate Research, Karlsruhe Institute of Technology, Karlsruhe, Germany*

²*Center for Climate System Research, Columbia University, New York, NY, USA; now at SRON Netherlands Institute for Space Research, Leiden, The Netherlands*

³*Department of Physics, The College of New Jersey, Ewing, NJ, USA*

⁴*Department of Chemistry, University of Puget Sound, Tacoma, WA, USA*

⁵*Laboratoire de Météorologie Physique, Université Clermont Auvergne/OPGC/CNRS, Clermont-Ferrand, France*

⁶*Department of Atmospheric Sciences, University of North Dakota, Grand Forks, ND, USA*

⁷*Institute of Methodologies for Environmental Analysis, National Research Council of Italy, Tito, Italy; and CommSensLab, Department of Signal Theory and Communications, Universitat Politècnica de Catalunya, Barcelona, Spain*

3.1. INTRODUCTION

Cirrus clouds are ubiquitous in Earth's atmosphere. At any given moment, they cover approximately 40–60% of Earth's surface and in the tropics the cirrus cloud coverage can reach up to 70% (e.g., Mace et al., 2009; Matus & L'Ecuyer, 2017; Sassen et al., 2008). Our understanding of cirrus clouds and their role in the climate system has improved greatly in the past decades thanks to new capabilities in modeling, improvements in remote sensing,

⁸*NASA Langley Research Center, Hampton, VA, USA*

increased accumulation of in situ data (e.g., with aircraft and balloon-borne measurements), dedicated laboratory and cloud chamber measurements, and development of new instrumentation. While it is generally agreed that cirrus clouds are an important cloud type both from climate and weather perspectives, it is also acknowledged that large gaps exist in our knowledge related to cirrus clouds, leading to substantial uncertainties and possible systematic biases in our predictions of Earth's future climate (Boucher et al., 2013).

Partly, these uncertainties arise from inadequate understanding of microscale physics. Based on data gathered with airborne cloud instruments, it is well known that cirrus ice crystals cover a wide range of crystal sizes from a few micrometers for newly formed crystals to several millimeter sized precipitation particles (e.g., Krämer et al., 2020). It is also known that, unlike spherical liquid droplets, cirrus ice crystals manifest impressively myriad geometries (e.g., Baran, 2009; Lawson et al., 2019). The basic shape of ice crystals often resembles a sixfold radial symmetry that can be attributed to the hexagonal molecular structure of ice. Three facets are most commonly observed: the basal, the prismatic, and the pyramidal. Laboratory studies have shown that the growth rates of these facets are determined by temperature and relative humidity leading to different crystal habits, such as columnar crystals, plate-like crystals, and bullet rosettes (Bailey & Hallett, 2002, 2004, 2009). Variations in atmospheric conditions and interactions with other crystals and supercooled droplets lead to more complex crystal structures. One commonly used scheme to classify ice crystals contains 80 classes for snow and ice (Magono & Lee, 1966).

Recently, we have become aware that the morphological diversity of ice crystals extends beyond the crystal habits. Technological developments in the past decades have made it possible to inspect the sub-micron scale structure of ice surfaces using electron microscope technology (Magee et al., 2014, 2020; Neshyba et al., 2013; Pfalzgraff et al., 2010) and by inspecting high-resolution light scattering patterns of individual ice crystals (Schnaiter et al., 2016; Ulanowski et al., 2006, 2014). These studies have confirmed that ice crystal sub-micron scale structures are present in wide range of environmental conditions both in laboratory grown crystals (Magee et al., 2014; Neshyba et al., 2013; Schnaiter et al., 2016; Voigtländer et al., 2018) and in natural clouds (Järvinen et al., 2018a; Järvinen et al., 2018b; Magee et al., 2020; Ulanowski et al., 2014), and that there is substantial variation of crystal structure within habit classes, specifically in the number and aspect ratios of their components (Fridlind et al., 2016; Um & McFarquhar, 2007; Um et al., 2015).

Ice crystal morphology plays an important role in the interactions with electromagnetic radiation. For example, most notable to the human eye are optical phenomena known as halos and parhelia frequently seen around the Sun or Moon, records of which date back at least to Aristotle (Tape & Moilanen, 2006). Such phenomena are readily explained by pristine hexagonal facets: the 22° halo, for example, can be understood as resulting from the passage of light rays through two non-neighboring prismatic facets. Microscopic structures on the crystal's surface lead to randomization of the reflection angles on the crystal boundary and, thus, suppress the visibility of these optical phenomena. It was estimated that the contribution by pristine crystals to the total scattering cross-section needs to be at least 10–40% for halos to be observable, depending on crystal shape (Forster et al., 2020; van Diedenhoven, 2014).

On a global scale, ice crystal optical properties, together with cirrus cloud fraction, height and ice water path define the cirrus cloud radiative effect (CRE). According to our current understanding, the cirrus and ice cloud globally and annually averaged top-of-the-atmosphere (TOA) CRE is slightly warming, at about 5 Wm^{-2} (Gasparini & Lohmann, 2016; Hong et al., 2016). However, there is a significant source of uncertainty related to the magnitude and even sign of the cirrus and ice cloud CRE due to uncertainty in cloud macro- and microphysical properties. General circulation models (GCMs) aim to predict cloud macro- and microphysical properties and the cirrus CRE in current and future climate states. Most models include schemes to diagnose vertically resolved cloud fraction and ice water path, while recent advances in cloud microphysical parameterizations also allow models to predict ice number concentrations and related ice sizes (del Genio et al., 1996; Morrison & Gettelman, 2008; Zhao et al., 2017). While these modeled ice cloud properties constrain the cloud optical thickness, spectral absorption, and emissivity relatively well, they do not constrain the ice crystal scattering properties, which are largely determined by ice crystal morphological properties, such as crystal size (Zhang et al., 1999), shape (Hong et al., 2009; Mishchenko et al., 1995; Macke et al., 1998; Yang et al., 2007; Zhang et al., 1999; Zhao et al., 2018), and ice crystal morphological complexity (Järvinen et al., 2018a; Yi et al., 2013).

For a more accurate estimation of the radiative effects of cirrus and ice clouds, a better knowledge of ice crystal morphological and optical properties as a function of cloud type, location, height, and temperature is needed. Moreover, existing and emerging new information needs to be synthesized to gain a better understanding of cirrus properties relevant for climate modeling and weather forecasting. Recent review papers have provided an overview

of cirrus observations and occurrence (Heymsfield et al., 2017), ice crystal sizes and cirrus ice water contents (IWCs) (Krämer et al., 2020), ice crystal habits (Lawson et al., 2019), optical properties (Yang et al., 2018), and developments in space-borne remote sensing capabilities (van Diedenhoven, 2018). However, a review of the emerging knowledge of ice crystal morphology at the nano- and microscale is still missing. Since it has been shown that ice crystal optical properties are sensitive to morphological complexity, such as surface roughness (e.g., Yang et al., 2013), it is important to summarize the work on ice crystal morphological complexity to facilitate consensus between laboratory, field, and theoretical work.

In this chapter, we give an overview of the current work on ice crystal morphological complexity and its effects on ice cloud optical properties. We report both laboratory and field observations of complex ice crystals and aim to unify the terminology used in the field. First, section 3.2 gives a qualitative overview of ice crystal nano- and microscale morphological features and introduces these in the context of size scale. We also present the different metrics used to quantify ice crystal morphological complexity in different applications. Section 3.3 summarizes how crystal complexity can be quantified using (1) optical microscopy, (2) high-resolution angular light scattering patterns, and (3) space-borne remote sensing methods and what we have learned of the link between the degree of crystal morphological complexity and environmental conditions using these methods. Section 3.4 discusses the effects of crystal complexity on the single-scattering properties of ice crystals. We give an overview of the methods used to describe the interactions between electromagnetic light and ice crystals, introduce the state-of-the-art optical models for complex ice crystals, and discuss in situ and remote sensing observations of ice crystal angular light scattering properties and ice cloud asymmetry parameter. Section 3.5 discusses how ice crystal optical properties are linked to the cirrus CRE, the magnitude of cirrus CRE as a function of cloud optical thickness and geographical location, and the uncertainty in CRE caused by ice crystal morphological complexity. Finally, we give a summary of the present knowledge in section 3.6 and give recommendations for future research directions in section 3.7.

3.2. ICE CRYSTAL MORPHOLOGICAL COMPLEXITY ACROSS SCALES

Here, we aim to give a comprehensive, albeit not exhaustive, overview of types of complexity found in natural ice crystals. One challenge in this regard concerns terminology: although most observed ice crystals are not

pristine in nature, there is no uniform terminology or classification for ice crystal morphological complexity. Several types of morphological complexity are identified from laboratory and field measurements, including facet roughness, atypical facet angles, hollowness, inclusion of air bubbles and aerosol particles, rounded surfaces, conjoined prisms, aggregation of single crystals, riming, fracturing of ice crystals in ice-ice collisions, and sublimation as well as post-sublimation regrowth of micro facets.

Since identifying different morphological complexity types on a single crystal is not always possible, a useful way of addressing this challenge is to organize morphological complexity according to its spatial scale, as shown in Figure 3.1. Relevant scales are nanoscale, which includes most of the facet roughness features, and microscale that contains complexity types visible in optical microscopy. Since often morphological complexity lies between nano- and microscale, it has been found appropriate to use the term “mesoscopic complexity” (not to be confused with “mesoscale” commonly used to indicate a scale between micro and macro, e.g., in meteorological applications) to describe features from ~100 nm to a few tens of micrometers (Järvinen et al., 2018b; Magee et al., 2014; Neshyba et al., 2013; Schnaiter et al., 2016). The terms mesoscopic complexity and “mesoscopic roughness” have been used in conjunction with cryoscopic scanning electron microscopy (CSEM) observations (Magee et al., 2014; Neshyba et al., 2013) and high-resolution light scattering patterns (Järvinen et al., 2018a; Järvinen et al., 2018b). Schmitt et al. (2016) used the term “complexity” to describe the transition from single crystals to complex (aggregated) particles as seen in airborne cloud particle imagers. Here, we suggest to use the term “morphological complexity” (later referred to as “complexity”) to describe any morphological deviation from that of a pristine, ideal hexagonal prism.

3.2.1. Types of Morphological Complexity

Figures 3.2 and 3.3 provide a glimpse of various morphological complexities that have been observed in atmospheric ice particles. When looking at laboratory or in situ images of natural ice particles (e.g., Fig. 3.3), it quickly becomes apparent that many distinct types of complexity occur, and several of these complexities are often seen overlaid on a single particle. Nearly all of these categories of complexity have been observed by multiple observing platforms and can be seen in a spectrum ranging from barely detectable to dramatically affecting the morphology of the entire particle or the geometry of the facet surfaces.

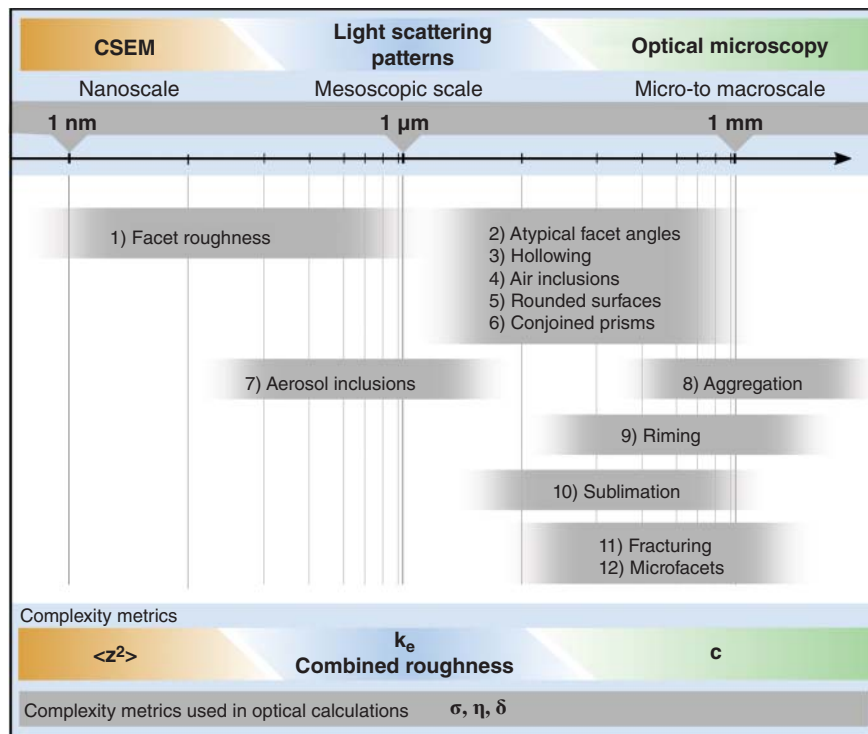


Figure 3.1 Overview of different types of ice crystal morphological complexity ranging scales from nano- to microscale and the methods to quantify crystal complexity in different scales: Cryoscopic scanning electron microscopy (CSEM), high-resolution light scattering patterns, and optical microscopy. The resulting complexity metrics can be divided into physical complexity metrics, which are the mean square of the local gradients of surface heights ($\langle Z^2 \rangle$) that can be retrieved from CSEM, the optical complexity parameters k_e and combined roughness that can be retrieved from high-resolution light scattering patterns, and the complexity parameter c that can be inferred from Cloud Imaging Probes, and to statistical complexity metrics that are used in computations to simulate the optical properties of ice crystals. The degree of facet roughness in the statistical methods can be described by width of the surface slope distribution specified by σ , η , or δ . A detailed discussion of the different complexity metrics can be found in section 3.2.2.

Facet Roughening

Ice crystal facets are frequently observed to be roughened – deviating from a flat, smooth planar surface. The characteristics of these deviations vary with respect to symmetry, scale, and geometric organization relative to the crystal lattice. For example, regular linear ridging is often observed running across prism facets, parallel with the basal plane (e.g., crystals 1b and 1c in Fig. 3.2 and Fig. 3.3. in Pfalzgraff et al., 2010). On basal facets, roughening is typically observed to be less symmetrically organized than on prism facets, sometimes with seemingly random roughening (crystal 1a in Fig. 3.2), and occasionally with dendritic patterning. It is also worth noting that this facet roughening is sometimes apparent in optical microscopy, but often only resolved by high magnification electron microscopy. Some facets reveal roughening at micron-scale, but others require nanoscale observational resolution to detect roughening

patterns. Notably, similar roughening patterns have been observed in both lab-grown ice crystals (Magee et al., 2014; Neshyba et al., 2013; Pfalzgraff et al., 2010) and captured cirrus particles (Magee et al., 2020). In addition, facet roughening has been observed during both growth and sublimation. Generally, growth mode roughening tends to appear more regular and symmetric relative to sublimation roughening.

Atypical Facet Angles

Atmospheric ice crystals also sometimes display crystal facet angles that diverge from a regular hexagonal polygons (Murray et al., 2015, and references therein). It is observed for ice crystals to present as “truncated triangles,” with alternating longer and shorter widths of prism facets (crystals 2 and 7 in Fig. 3.2). Although apparently less common, ice particles with rectangular or rhombic faceting have been observed as well. The frequency of

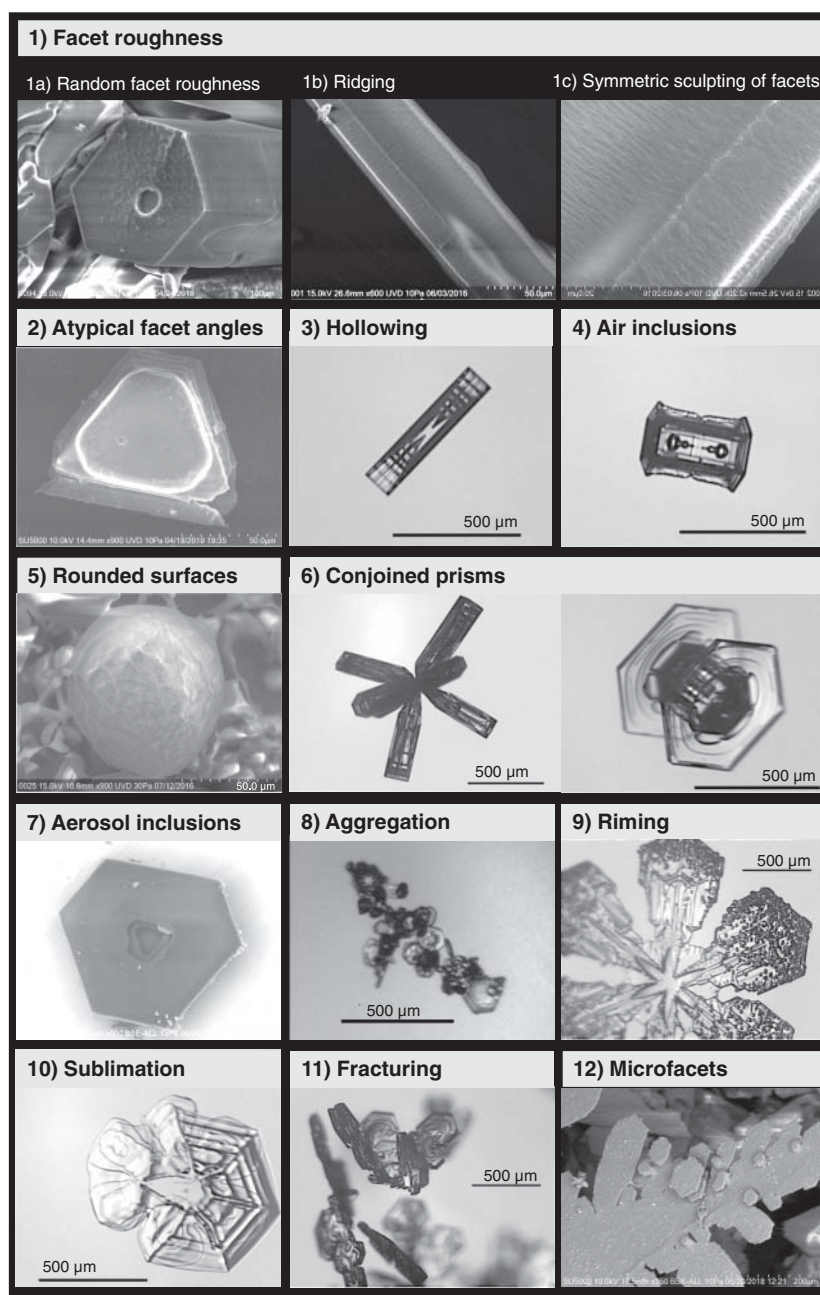


Figure 3.2 Examples of different types of morphological complexity seen on individual ice crystals. Example crystals 1, 2, 5, 7, and 12 were grown under CSEM and crystals 3, 4, 6, 8, 9, 10 and 11 were captured in situ in ice clouds.

these atypical particle symmetry under various atmospheric conditions is still uncertain, though in some samples, it may approach $\sim 25\%$ of crystals (Table 3.1).

Hollowing

Some degree of hollowing of ice crystals appears to be the rule rather than the exception in atmospheric ice

particles. While pristine hexagonal plates and columns with no apparent hollowing are observed in the atmosphere, they have been reported infrequently. Schmitt & Heymsfield (2007) reported fractions up to 80% of hollow ends in bullet rosette and columnar crystals in midlatitude cirrus with hollow-fraction increasing with column and bullet length, and Walden et al. (2003) reported that

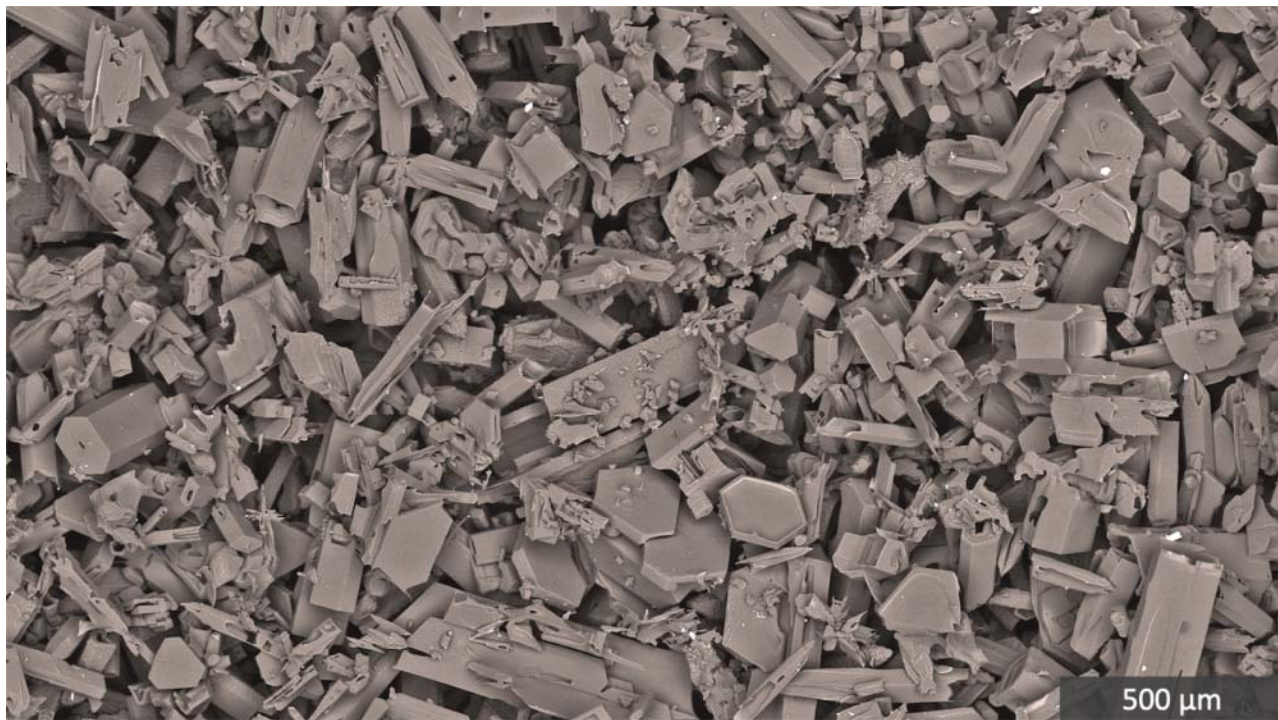


Figure 3.3 Approximately 500 cirrus ice particles captured from near the top of a synoptically forced cirrus cloud at ~ 11 km altitude, and temperature -50°C . Particles from this single cloud top show many different habits and multiple types of complexity (e.g., facet roughening, atypical facet angles, hollowing, rounded surfaces, conjoined prisms, aerosol inclusion, sublimation, fracturing, and microfacets).

all bullet-shaped ice crystals and most columns were frequently hollow in precipitation at South Pole. As with all categories of observed ice particle complexity, hollowing is observed in a spectrum from being barely noticeable to having profound impacts on particle geometry. Some particles show slight depressions and pits on facets (e.g., example crystals 1a, 2, and 7 in Fig. 3.2), while other particles demonstrate sheath-like hollowing that extends through the length of the particle (example crystal 3 in Fig. 3.2). Recent work by Nelson & Swanson (2019) demonstrates images and mechanics of the early formation stages of hollowing and air inclusions on lab-grown ice crystals, which develop through thin layers of laterally protruding growth, sourced from a flux of surface-mobile molecules.

Air Inclusions and Air Pockets

Ice crystals with air inclusions or air pockets are thought to be common in cirrus clouds. The inclusion of air bubbles or pockets adds to the ice crystal complexity and can significantly affect ice crystal optical properties (Hong & Minnis, 2015; Macke, Mishchenko, et al., 1996; Tang et al., 2017; Xie et al., 2009). Modeling studies have suggested that both facet roughness and air inclusions are needed to explain polarimetric satellite observations (Tang et al., 2017). Air inclusions can either form when

air dissolved in the liquid phase gets trapped in the heterogeneous freezing process (Maeno, 1967) or when a liquid water layer forms enveloping the ice crystal and is incorporated when the layer freezes. Nelson & Swanson (2019) studied the formation of pockets (corner pockets, planar pockets, and elongated edge pockets) in laboratory generated ice crystals. Pockets were formed when a sublimated ice crystal was regrown, where the process was largely driven by surface transport across the boundary of a face to the advancing edge. Therefore, occurrence of pockets in atmospheric ice crystals can give evidence of sublimation and regrowth cycles.

Occurrence of Rounded Surfaces

Rounded surfaces are also frequently found on atmospheric ice particles, originating from several apparent mechanisms. Ice particles that nucleate from small droplets will initially retain a nearly spherical droplet shape, although other surface roughness may still be layered on the rounded surface (see crystal 5 in Fig. 3.2). Freezing of small droplets to quasi-spherical shapes has been frequently reported in convective cirrus (e.g., Järvinen et al., 2016) and in ice fog situations (Schmitt et al., 2013). Of course, these drops will often then form the nucleus of a faceted single ice crystal or poly-crystalline particle that grows by vapor deposition (“droxtals”), but

the transition from rounded to faceted may sometimes proceed slowly, incompletely, or not at all, depending on the local temperature and saturation regime (Gultepe et al., 2017). Another common observation of rounded surfaces occurs with highly sublimated ice particles (see crystal 10 in Fig. 3.2). Although perhaps less recognized, it is important to note that some sublimation conditions have been observed to lead to complex, sharp asperities on ice surfaces. Further research is necessary to distinguish between the circumstances that lead to sublimation rounding or sublimation roughening. An additional category of rounded ice surfaces has been observed to occur in actively growing single crystals, in a zone intermediate between faceted basal and pyramidal planes (e.g., Fig. 1 in Pfalzgraff et al., 2010).

Conjoined Prisms

Complex ice particles that appear as “conjoined prisms” are very frequently observed in natural cirrus and mixed-phase clouds. These conjoined prisms may sometimes be single crystals with highly variable aspect ratios (capped columns a.k.a. “TIE-fighters,” see crystal 6b in Fig. 3.2), though most commonly, conjoined prisms appear as polycrystals growing from a common nucleation nexus. Bullet rosettes (see crystal 6a in Fig. 3.2) are the most well-recognized manifestation, though polycrystals with plate-dominated aspect ratio, and particles with mixed aspect ratio also appear regularly (Bailey & Hallett, 2009). There is some suggestion that the frequency of such mixed or planar polycrystals may be somewhat under-appreciated since they may sometimes be classified as “irregular” by automated categorization schemes (Stoelinga et al., 2007).

Aerosol Inclusions

The importance of understanding the role of ice-protect nucleating aerosol particles has long been recognized as a key issue in atmospheric ice clouds. Chapter 2: An overview of aerosol-cloud interactions provides a more complete description of ice crystal formation upon aerosol surfaces. However, relatively less attention has been paid to the scavenging of aerosol particles by ice crystals. Small aerosol particles (nm to μm scales) embedded or adhered to ice surfaces are typically not resolvable by airborne cloud particle imaging probes, but recent CSEM results suggest that adhered and included aerosols on ice crystals are common (Magee et al., 2020). Initial results suggest that the mean density of aerosol inclusions is highly variable, and likely dependent on air mass origins. Furthermore, as ice particles undergo a large degree of sublimation and erosion, adhered aerosols tend to aggregate toward the particle center, and gradually come to dominate the mass of the particle as the ice approaches complete sublimation. As with riming, such aerosol

particles also often appear to be affected by particle aerodynamics, adhering in greatest density near particle corners (see crystal 7 in Fig. 3.2). Energy dispersive X-ray spectroscopy (EDX) promises to aid in measuring the chemical composition of the aerosol particles.

Aggregation

Most frequently associated with the formation of snowflakes in precipitating mixed-phase clouds, aggregation has been occasionally observed in mixed-phase and ice clouds. The occurrence of aggregated particles appears to decrease with decreasing temperature, particle number concentration, and particle size (Schmitt et al., 2016); however, several observers suggest that charged ice particles may aid in the formation of ice particle chains in cirrus clouds with significant electrification, for example, in convective anvils (see crystal 8 in Fig. 3.2 and Connolly et al., 2005; Stith et al., 2014).

Riming

Riming describes the accretion of small, supercooled liquid droplets on the surface of atmospheric ice particles (see crystal 9 in Fig. 3.2). It is most significant in mixed-phase precipitation-bearing clouds. However, the riming process may also play a significant role in amplifying complexity of ice particles within liquid-origin cirrus clouds and appears likely to contribute potential origin-points for new growth of microfacets.

Sublimation

Atmospheric ice crystals first nucleate, then subsequently grow and sublimate, sometimes cycling through multiple cycles of growth and ablation. It is therefore not surprising that observations of atmospheric ice crystals frequently evince marked indications of the sublimation process. Frequently, sublimation appears to result in smooth, rounded edges compared to the sharp edges of actively growing crystals (see crystal 10 in Fig. 3.2). However, exceptions to this rule have been observed in both directions. For example, on occasion, sublimation has been observed to yield a facet surface of apparently randomly sharpened ridges and peaks, and also to contribute to patterned roughening in the form of sculpted facet ridging. Conversely, actively growing ice crystals can also present smooth surfaces (see rounded surfaces above).

Fracturing

Ice-ice collisions, complementary to the formation of aggregates, lead to the breaking-up of individual ice crystals (e.g., Takahashi, 1993). Fracturing is most frequent on relatively large particles ($D \geq 1 \text{ mm}$) such as dendrites and previously aggregated or rimed crystals. Further, fracturing can also take place during the sublimation process or be the result of cracking during the freezing of supercooled liquid droplets (e.g., Lauber et al., 2018).

Table 3.1 Summary of different complexity types, the typical temperature (T) range they form, expected ice saturation conditions, and estimation of their frequency.

Complexity type	Typical T range	Sub- or supersaturated conditions	Frequency	References
Facet roughening	Across all temperatures	Both	Always present	Pfalzgraff et al. (2010); Neshyba et al. (2013); Magee et al. (2014, 2020)
Atypical facet angles	Usually in $T < -70^{\circ}\text{C}$ but also observed in precipitation	Both	Frequent (up to 25%)	Murray et al. (2015, and references therein)
Hollowing	Across all temperatures	Both	Very frequent (up to 80%)	Schmitt & Heymsfield (2007); Nelson & Swanson (2019)
Air inclusions and air pockets	Across all temperatures	Both ^a	Frequent	Maeno (1967); Nelson & Swanson (2019)
Occurrence of rounded surfaces	Usually $T < -50^{\circ}\text{C}$	Mostly sub-saturated	Frequent	Pfalzgraff et al. (2010); Schmitt et al. (2013); Järvinen et al. (2016)
Conjoined prisms	-20 to -50°C	Both	Very frequent	(Bailey & Hallett, 2009; Lawson et al., 2019)
Aerosol inclusions	Across all temperatures	Both	Uncertain	Magee et al. (2020)
Aggregation	Usually $T > -40^{\circ}\text{C}$	Both	Frequent	Connolly et al. (2005); Schmitt et al. (2016)
Riming	$T > -38^{\circ}\text{C}$ (when liquid droplets are present)	Both	Frequent	Ono (1969); Hallett & Mossop (1974); Mosimann et al. (1993); Avila et al. (2009)
Sublimation	Across all temperatures	Sub saturated	Frequent	
Fracturing	Around -15°C	Both	Not so frequent	Takahashi (1993); Lauber et al. (2018)
Microfacets	Uncertain	Both ^a	Frequent	Neshyba et al. (2013); Magee et al. (2014, 2020)

^a Potential indication of growth and sublimation cycles.

Microfacets

The growth of small new facets upon larger, preexisting ice crystal facets that can match the preexisting lattice structure of the underlying crystal appears to occur with some frequency in both mixed-phase and ice clouds. Rimed cloud droplets from mixed-phase clouds adhered onto ice particles seem to serve as a potential re-nucleation points (see crystal 12 in Fig. 3.2). Perhaps more pervasively, repeating cycles of growth and sublimation may lead to microfaceting, with each phase cycle contributing to increasing particle complexity (Voigtländer et al., 2018).

3.2.2. Complexity Metrics

Several metrics describing the degree of morphological complexity at various scales have been proposed and

used in the literature. Such metrics can be divided into two categories, namely (1) physical complexity metrics derived from CSEM images, high-resolution light scattering patterns, or optical microscopy, and (2) optical complexity metrics used to simulate the optical effects of ice crystal complexity. Here, we give an overview of the two categories.

Physical Complexity Metrics

An extensive assembly of parameters describing surface roughness has been defined in industrial settings. The ISO Standard 25178, for example, defines parameters representing the distribution of heights above a reference plane, the periodicity, anisotropy, and curvature of features within that plane, void volumes, and many others. Different parameters have become established in various fields. For example, in optical engineering

applications the root mean square roughness σ_{rms} is of particular interest and widely used for the quantification of diffuse light scattering from “smooth” optical grade surfaces. By contrast, ice surface morphology research has had a much more narrow focus, emphasizing the local gradients of surface height in the horizontal directions, Z_x and Z_y , and its square, $Z^2 = Z_x^2 + Z_y^2$. Two statistical properties of Z^2 , moreover, have received the most focus in ice research: its mean, designated here as $\langle Z^2 \rangle$, and its standard deviation, designated σ .

A few points about this focus are worth emphasizing here. First, the reason for the emphasis on Z_x and Z_y is the close connection between their distribution and the angles of incidence and refraction and reflection of light impinging on a textured, but otherwise planar, surface. This relationship may be obtained by Snell’s law when the wavelength of light is much smaller than the spatial scale of surface texture. Second, the primary reason for limiting focus to statistical properties $\langle Z^2 \rangle$ and σ is practical rather than fundamental: most available sources of information, for example, the optical scattering properties of surfaces, do not justify a more detailed description. Recent CSEM work is beginning to provide more detailed information, for example, about the kurtosis, skewness, and so on of these distributions, and such work has itself brought up fundamental questions, especially about the spatial scale of the roughness, that have yet to be resolved. A third point concerns the relationship between $\langle Z^2 \rangle$ and σ on one hand, and model (analytical) distributions of the gradient. For example, while $\langle Z^2 \rangle$ and σ may (and do) form the basis of parameterizations of such models (see, e.g., the dependence of Weibullian σ_{wb} and η , Butterfield et al. (2017)), they derive from the actual distribution of Z^2 , and therefore stand independently of such models and their parameterizations.

In many applications, the degree of morphological complexity is measured indirectly, for example, by measuring the distribution of scattered light around a specular reflection (Lu et al., 2006). Such methods are used in industrial settings for probing the quality (or smoothness) of produced surfaces and, lately, have found their way into atmospheric sciences. The degree of complexity of three-dimensional (3-D) individual ice crystals can be quantified from high-resolution light scattering patterns measured using the Small Ice Detector Mark 3 (SID-3) instrument (Schnaiter et al., 2016; Ulanowski et al., 2014). Examples of SID-3 scattering patterns of individual ice crystals with different degrees of complexity can be seen in Section 3.3. The degree of complexity is related to the image texture of the measured light scattering patterns that are analyzed using a gray-level co-occurrence matrix (GLCM) method (Lu et al., 2006). GLCM is a frequency matrix describing how often pairs of gray levels occur in a texture image for pixels separated

by a certain distance Δd and along a certain direction. Speckle pattern texture features can then be extracted from the GLCM. For analyzing ice crystal complexity, the relevant texture features are “combined roughness” (Ulanowski et al., 2014) and the “normalized energy feature parameter” (k_e) (Lu et al., 2006; Schnaiter et al., 2016). The combined roughness is weighted so that has bounds between 0 and 1 for most particles whereas k_e approximately varies between 4 and 6. Although both combined roughness and k_e have been shown to correlate with actual physical surface complexity (Schnaiter et al., 2016), there is no unequivocal link between these parameters and $\langle Z^2 \rangle$ or σ . Also, it should be noted that this method is sensitive to all types of complexities with scales around the wavelength of the incident light (see Fig. 3.1) so discrimination between different types of complexities discussed in section 3.2.1 is not possible.

Whereas the previously introduced metrics describe crystal complexity at the nano- and mesoscopic scales, Schmitt & Heymsfield (2014) introduced a unitless complexity parameter C that describes crystal complexity in micro- and macroscale derived from ice crystal microscopic images observed by the cloud particle imaging (CPI) probe. The complexity parameter C is inferred from a combination of the area of the circle with the smallest area that covers the particle, the projected area of the particle, and the perimeter of the particle. Schmitt et al. (2016) showed that C generally increases with particle size and the number of monomers in an aggregate particle.

Optical Complexity Metrics

Complexity metrics in category (2) are used in combination with computational methods to simulate the optical properties of ice crystals (see more details on light scattering models in section 3.4.1). They can be divided into methods that generate the optical effect of complexity (a) by using the tilted-facet (TF) method, where the normal of the crystal facet surface is tilted randomly from its nominal orientation, (b) by generating complex, randomized morphologies, or (c) by simulating the bidirectional scattering distribution function (BSDF) around the specular reflected and the transmitted ray direction. Although method (c) is mainly used in the field of technical optics, we will show in section 3.4.2 how this knowledge could be transferred into the field of ice crystal light scattering.

The TF approach (a) is generally applicable to simulations of ice optical properties based on geometric optics. For example, Macke et al. (1996) used a set of random tilt angles distributed uniformly between $[0, \theta_t^{\text{max}}]$ to specify the degree of complexity caused by facet roughness or crystal distortion, where the degree of complexity is defined as

$$\delta = \theta_t^{\text{max}} / 90^\circ. \quad (3.1)$$

Yang & Liou (1998b) specified the degree of surface complexity caused by facet roughness using a first-order Gram-Charlier density function (i.e., Gaussian distribution) motivated by Cox & Munk (1954) who studied the optical effect of sea surface roughness. Here, the facets are tilted randomly according to the distribution

$$P(Z_x, Z_y) = \frac{1}{\sigma_g^2 \pi} \exp\left(-\frac{Z_x^2 + Z_y^2}{\sigma_g^2}\right), \quad (3.2)$$

where (as described above) Z_x and Z_y are local gradients of the surface height in the x and y directions and σ_g is a complexity parameter controlling the degree of roughness. Figure 3.4 shows three examples of hexagonal ice crystals with varying degree of complexity generated using equation (3.2).

Later, Shcherbakov et al. (2006) introduced a more general Weibull distribution to the TF approximation, namely

$$P(Z_x, Z_y) = \frac{1}{\sigma_{wb}^2 \pi} \left(\frac{Z_x^2 + Z_y^2}{\sigma_{wb}^2}\right)^{\eta-1} \exp\left[-\left(\frac{Z_x^2 + Z_y^2}{\sigma_{wb}^2}\right)^\eta\right], \quad (3.3)$$

where σ_{wb} is the complexity parameter and η is an additional shape parameter in the Weibull distribution. If $\eta = 1$, then equation (3.3) reduces to equation (3.2).

Simulations implementing the TF method have shown that ice crystal optical properties are largely equivalent regardless of used optical complexity metrics (Geogdzhayev & van Diedenhoven, 2016; Neshyba et al., 2013). Therefore, the TF method has been used to simulate the optical effects of complexity across multiple scales from facet roughness (Liu et al., 2013; Macke, Mueller, et al., 1996) to internal structures, such as air inclusions (Hong & Minnis, 2015; Macke, Mishchenko et al. 1996), to macroscale complexities, such as aggregation (Letu et al., 2016).

The approach (b) to simulate the optical effect of complexity is to generate complex, randomized morphologies. Examples of complex morphologies used for ice crystals are Koch fractals (Macke, Mueller, et al., 1996), Voronoi particle (Letu et al., 2016), Gaussian roughness on random spheres (Nousiainen & McFarquhar, 2004; Nousiainen & Muinonen, 2007; Um & McFarquhar, 2011), and particles prescribed by Chebyshev polynomial series (McFarquhar et al., 2002) and superspheroids

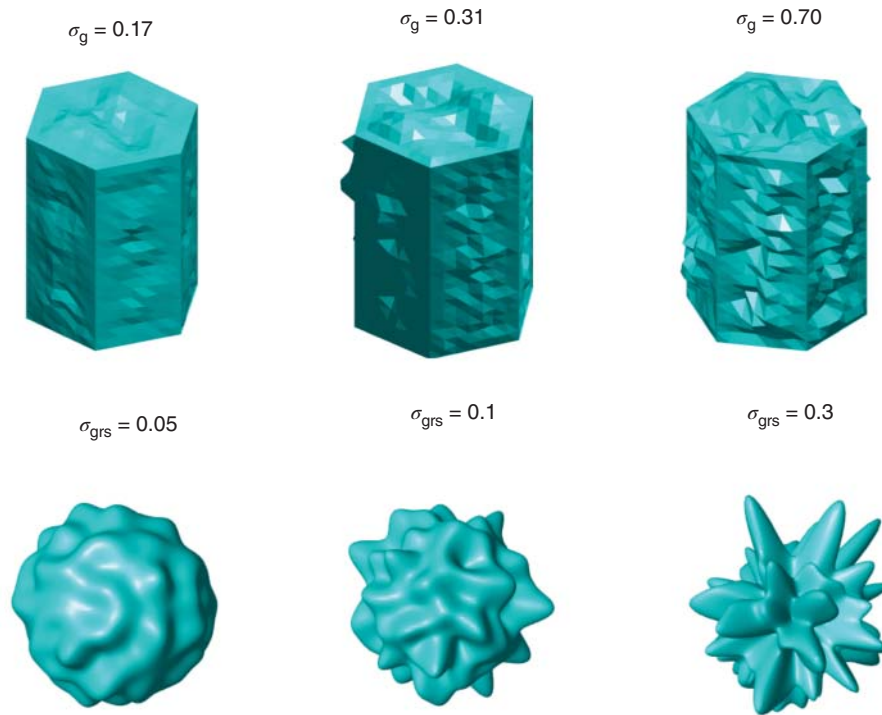


Figure 3.4 Roughened hexagonal columns and Gaussian random spheres with different degree of complexity. Note that the roughened hexagonal column is an illustration of the physical manifestation of complexity generated by the TF approach. In the actual ray-tracing calculation, the whole facet is tilted when encountered by the ray so that geometrical optics assumption is valid.

(Sun et al., 2022). These approaches all include parameters that alter the shapes, and which may be interpreted as complexity metrics. For example, the shape of the Gaussian random sphere geometry is described by a covariance function of radius as follows:

$$\mathbf{r}(\vartheta, \varphi) = \frac{a}{\sqrt{1 + \sigma_{\text{grs}}^2}} \exp[s(\vartheta, \varphi) \hat{\mathbf{e}}_r] \quad (3.4)$$

where a is the mean radius, σ_{grs} is the relative standard deviation of radius controlling the degree of complexity, s is the so-called logradius, and $\hat{\mathbf{e}}_r$ is a unit vector in spherical coordinates. Examples of Gaussian random spheres with different degree of complexity are shown in Fig. 3.4. A downside of such approaches is that the morphologies are generally inconsistent with general hexagonal structure of ice and may not be considered realistic for natural ice crystals. Therefore, limited calculations have been performed for hexagonal prisms with randomized roughness structures added to their surfaces (Collier et al., 2016; Liu et al., 2013). A benefit of some of these approaches is that they are applicable to methods to calculate the optical properties for small size parameters (i.e., small ice crystals and/or at long wavelengths) for which the geometric optics, and thus the TF approach, cannot be applied (Kahnert et al., 2012; Nousiainen & Muinonen, 2007).

The approach (c) is used in technical optics to describe the residual light scattering of optical grade surfaces and is available in most optical design and engineering ray-tracing software. The broadening of the specular reflection and transmission peaks is described using, for example, the *ABg* model (Pfisterer, 2011). Based on scalar diffraction theory, these types of model are parameterized to describe the angular dependency of radiant power that is scattered out of the specular and transmitted rays. The *ABg* model is defined as

$$\text{BSDF}(\beta - \beta_0) = \frac{A}{B + (\beta - \beta_0)^g} [\text{sr}^{-1}], \quad (3.5)$$

where BSDF, the bidirectional scattering distribution function, is the ratio between scattered and incident power, $\beta = \sin(\theta_{\text{scattered}})$, $\beta_0 = \sin(\theta_{\text{specular}})$, A/B the diffuse scattering fraction in the peak direction, and g the slope with which the power decreases away from the specular and transmitted beams. $B^{1/g}$ then defines the rollover angle where the BSDF starts to change from a constant (Lambertian) angular dependency to a power law decrease for larger angles. This angle is typically less than a degree. The *ABg* model is valid if the surface roughness is isotropic and the root mean square roughness parameter σ_{rms} is of the order of the incident wavelength or less (commonly only a few %). Therefore, the *ABg* model can be used to describe sub-micron scale facet roughness when performing measurements with visible light.

While the aforementioned optical complexity metrics (a–c) are introduced to simulate the optical effects of complexity, recently, Xu et al. (2022) introduced a complexity metric that can be derived from the angular scattering function due to the *reflection – refraction* of light rays, namely, the C_p parameter, defined as follows:

$$C_p = \left(\sum_{l=0}^{\infty} |\hat{c}_{GO,l}| \right)^{-1}, \quad (3.6)$$

where $\hat{c}_{GO,l}$ are the expansion coefficients of the angular scattering function using Legendre polynomials. It is found by Xu et al. (2022) that this parameter is strongly correlated with the distortion parameter δ introduced by Macke et al. (1996), and potentially with other complexity metrics as well because these complexity metrics (a–c) often lead to similar effects on phase function. A significant advantage of this approach is that the C_p parameter is retrievable by polar nephelometers, making the comparisons among models and measurements quite convenient.

Linking Physical and Optical Complexity Metrics

As our capabilities to observe and quantify physical complexities of ice crystals continue to grow, it is becoming increasingly important to establish “crossover” linkages between the aforementioned physical and optical complexity metrics. Apart from providing a more comprehensive picture of complexity, such linkages could be used in the service of broader objectives, for example, to clarify how cirrus CREs might respond to changes in environmental conditions and climate, or to improve the information obtained from remote sensing algorithms.

This goal remains an active area of research. Schnaiter et al. (2016) attempted to link the SID-3 complexity parameter k_e to the distortion parameter σ_{grs} describing the distortion in the Gaussian random sphere model introduced above (equation (3.4)). They used ADDA/GDT-matrix approach to simulate SID-3 scattering patterns and analyzed these patterns using the GLCM. A clear correlation between k_e and σ_{grs} was found, where a k_e of 4.6 corresponded to a significant σ_{grs} of 0.3. k_e was saturated at σ_{grs} value of 0.5. Since the study was restricted to relatively small crystal sizes of 7.8 μm (due to computational limitations) and to a single non-hexagonal crystal shape (Gaussian random sphere), more work along these lines is required to reach a comprehensive crossover between k_e and optical parameterizations. In a similar vein, Neshyba et al. (2013) showed that the sensitivity of the 22° halo to ice crystal complexity depends crucially on the symmetry of prismatic-facet roughening: when that roughening is azimuthally anisotropic (occurs in rows), the halo is degraded to a far less extent than when

the roughening is azimuthally isotropic; both symmetries have been observed in real cirrus clouds, although the environmental conditions that control their occurrence are unknown.

3.3. OBSERVATIONS OF COMPLEX CRYSTALS

In this section, we summarize how crystal complexity has been quantified using (1) CSEM methods and optical microscopy, (2) high-resolution angular light scattering patterns, and (3) space-borne remote sensing observations. Methods (1) and (2) have been applied both for laboratory-grown and in situ ice crystals. We also discuss what we have learned so far about the link between ice crystal complexity and prevailing environmental conditions.

3.3.1. Microscopic Observations of Ice Morphology Associated with Complexity

Here, we summarize what is known about the morphologies of surface complexity at the nano- and mesoscopic scales. The methods underpinning these observations may be divided into field observations versus laboratory measurements on the one hand, and high-resolution optical microscopy versus CSEM on the other hand. We will briefly consider insights from these in various combinations.

Considering first the category of field optical microscopy (e.g., Walden et al., 2003), it is evident that complexity in naturally occurring ice crystals is strongly influenced by the underlying crystal symmetry. For example, both the surface texturing appearing in crystal 10 in Fig. 3.2 and the hollowing in crystal 3 in Fig. 3.2 clearly respect the sixfold crystal symmetry of the basal facet. (Indeed, it is tempting to speculate that hollowing of basal facets is an extreme form of symmetric basal surface texturing.) Crystal 3 in Fig. 3.2 also hints at another symmetry, appearing as lines running perpendicular to the long (crystallographic) *c* axis; however, it is not clear from this image whether this is a feature of the outer surface of the prismatic facets, or of the inner (hollowed) surface. Field-obtained optical images have also shown the existence of myriad other forms of complexity, for example, the conjoined prisms, riming, aggregation, and fracturing shown in Fig. 3.2.

A second category of investigation, laboratory studies using optical microscopy, offers the possibility of performing growth and ablation experiments through the manipulation of environmental variables. Such studies have revealed the occurrence of air inclusions, the compounding effects of multiple growth/ablation/regrowth cycles, and insights into the mechanisms by which crystal

facets increase in area (Bacon & Swanson, 2000; Nelson & Swanson, 2019).

A third category of investigation is CSEM studies of laboratory-grown ice (Magee et al., 2014; Pfalzgraff et al., 2010). This approach is capable of providing greater surface detail than is possible with optical microscopy, albeit at the price of losing the ability to peer into a crystal, since CSEM is a surface-only technique. The aforementioned twofold symmetry appearing in crystal 3 in Fig. 3.2 is frequently observed in CSEM images of ice, where it is unambiguously attributable to texturing on the outside surface of prismatic facets (Pfalzgraff et al., 2010, see also examples in panels 1b and 1c). CSEM work has also shown that non-symmetrical (i.e., random) sculpting regularly occurs on facets of all types, sometimes in combination with symmetric roughening, and sometimes not (see crystals 1a–c in Fig. 3.2). The quantitative topographical capability of CSEM (which so far has not been worked out for optical microscopy of ice) has proven a key asset in this regard (Butterfield et al., 2017). Such work has revealed, for example, that the vertical relief of facet roughening, while typically not more than a few micrometers, tends to be larger for symmetric roughening than for non-symmetric roughening. Model representations invested with explicit, CSEM-derived surface topologies offer the additional advantage of permitting study of the light scattering properties in a more realistic way than Gaussian or Weibull (i.e., random-variable) methods permit (Neshyba et al., 2013) (described in more detail in section 3.4.1).

A fourth category is CSEM studies of ice captured in the field (Magee et al. (2020); see Fig. 3.3 for an example). This approach provides unique insights into the diversity of real-world ice crystal complexity (e.g., facet roughening, atypical facet angles, hollowing, rounded surfaces, conjoined prisms, and aerosol inclusion), and offers the possibility of guiding laboratory experiments seeking mechanistic origins of these forms of complexity.

3.3.2. Deriving Mesoscopic Complexity from High-Resolution Angular Light Scattering Patterns

Ice crystal mesoscopic complexity of small ice crystals in the sub-50 μm size range can be investigated by analyzing high-resolution angular light scattering patterns measured with the SID-3 instrument as discussed in section Physical Complexity Metrics. This method has been applied for laboratory-generated ice crystals and ice analogue particles (Schnaiter et al., 2016; Ulanowski et al., 2006; Voigtländer et al., 2018), and to investigate the mesoscopic complexity of cirrus ice crystals in airborne studies over midlatitudes (Järvinen et al., 2018b; Ulanowski et al., 2014) and the tropics (Järvinen et al., 2018a).

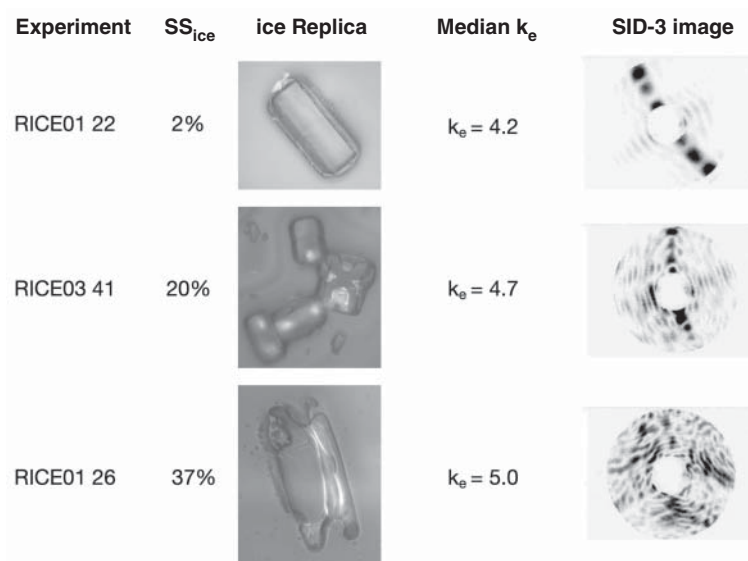


Figure 3.5 Examples of ice crystal replicas sampled during three crystal growth experiments performed at the AIDA cloud chamber. Ice crystals were grown in three different supersaturation conditions where the median ice supersaturation (SS_{ice}) was 2%, 20%, and 37%. The resulting ensemble median complexity parameters (k_e) were 4.2, 4.7, and 5.0, respectively. The SID-3 images show a representative scattering pattern for a single ice crystal from the same experiment having a complexity parameter corresponding to the median complexity parameter of the crystal ensemble. All ice crystals were below 100 μm .

Schnaiter et al. (2016) performed a series of laboratory experiments at the Aerosol Interactions and Dynamics in the Atmosphere (AIDA) cloud chamber where ice crystals were grown and sublimated at defined super- and subsaturated ice conditions at the cirrus temperature range between -40 and -60°C . The mesoscopic complexity of the ice crystals was quantified using the complexity parameter k_e as defined in section Physical Complexity Metrics. Figure 3.5 shows a visualization of ice crystal replicas from three of the experiments and a representative single-particle high-resolution angular light scattering patterns. The examples show that increase in ice supersaturation during growth is accompanied by visual increase in hollowing of the crystals. Note that conclusions about facet roughness cannot be made in the replicas. The single-particle high-resolution scattering patterns reflect this change so that increase of the number and decrease of the size of the speckles are seen in the images leading to an increase in k_e . In the AIDA experiments, a linear dependency was found between the growth ice supersaturation and the complexity parameter k_e for one temperature range in case of heterogeneously nucleated ice crystals. Figure 3.6 shows the fit to the laboratory measurements. It can be seen that only complex crystals ($k_e > 4.6$ or $\sigma_{grs} > 0.3$) were generated in experiments with starting temperature of 233 K, whereas at a colder starting temperature of 225 K ice crystals with complexity parameters below 4.6 were grown at ice

supersaturations below 20%. Ice crystals with complexity parameter below 4.6 are considered as optically “pristine” so that the spatial light scattering is mainly defined by the habit and not crystal complexity, that is, showing a lack of speckles (see Fig. 3.5).

Similarly, Voigtländer et al. (2018) investigated how combined roughness parameter was affected by crystal growth conditions using the Ice Roughness Investigation System (IRIS) laboratory setup. They also found that, under laboratory conditions, complexity parameter correlates with the crystal growth conditions so that a higher saturation ratio with respect to ice led to higher complexity parameters. Furthermore, Voigtländer et al. (2018) found that repeated growth and sublimation cycles led to a memory effect and gradual “ratcheting up” of crystal complexity.

Despite the evidence from laboratory experiments showing that complexity parameters correlate with crystal growth conditions, no clear correlation between complexity parameters and simultaneously measured environmental variables has been found in natural cirrus clouds using the SID-3 method (Järvinen et al., 2018b; Ulanowski et al., 2014). This is also summarized in Fig. 3.6 that shows re-analysis of SID-3 data from two airborne campaigns from the tropics (ACRIDICON-CHUVA) and from the midlatitudes (ML-CIRRUS) containing both convective and in situ cirrus. The measured k_e values are grouped into four temperature bins and shown as a

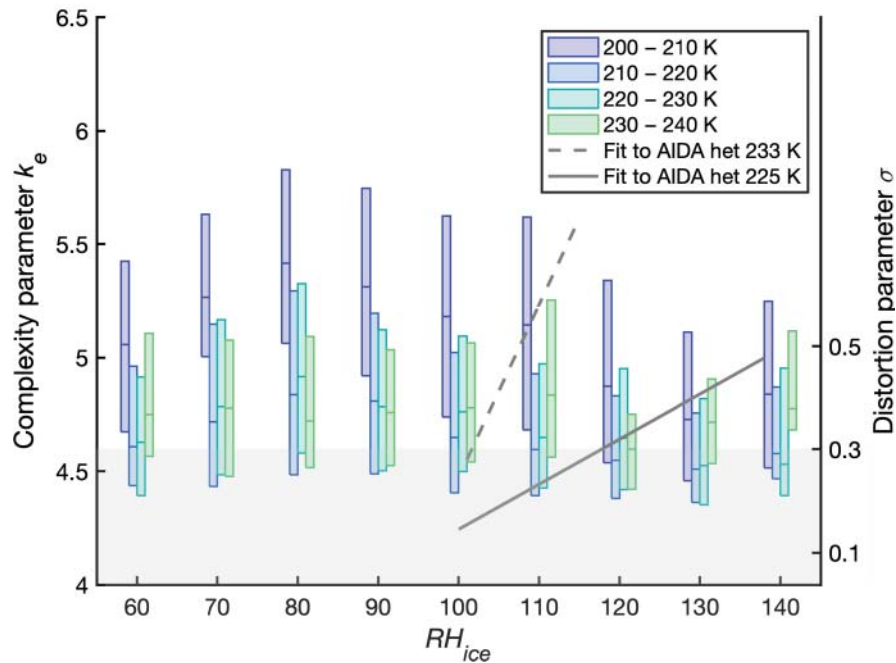


Figure 3.6 Statistical analysis of ice crystal complexity values retrieved from SID-3 measurements collected during the Midlatitude CIRRUS (ML-CIRRUS) and the ACRIDICON-CHUVA campaigns. The boxes represent the interquartile range for different temperature ranges and the line represents the median values. The gray solid and dashed lines represent the linear dependency that was observed in cloud chamber simulation experiments for heterogeneously nucleated ice crystals with initial chamber temperatures of 233 K (dashed line) and 225 K (solid line). The shaded gray area (below $\sigma \leq 0.3$) illustrates the range of k_e values where the ice crystals can be considered to be optically pristine. Source: Adapted from Schnaiter et al. (2016) and Järvinen et al. (2018a).

function of simultaneously measured relative humidity with respect to ice (RH_{ice}). The data were originally published in Järvinen et al. (2018a). Although no clear trend is seen in the median complexity parameters as a function of simultaneously measured RH_{ice} , some trend toward higher complexity values in the lowest temperature bin (200–210 K) in compared to higher temperatures is seen. Also, on average higher complexity values are found in subsaturated ($RH_{ice} < 100\%$) conditions compared to conditions where $RH_{ice} > 100\%$, which could indicate that sublimation can increase complexities as suggested by CSEM studies. In general, atmospheric measurements with the SID-3 instrument have shown a high degree of ice crystal complexity independent of the measurement location, cirrus type, or even cloud type (cirrus or mixed-phase cloud) (Järvinen et al., 2018a).

Understanding the origin of crystal complexity in natural ice clouds is a topic of ongoing research (see section 3.7). Since SID-3 observations are limited in geographical location and crystal size, other methods are needed to overcome these limitations, such as remote sensing techniques reviewed in the next section.

3.3.3. Remote Sensing of Ice Crystal Complexity

Multi-angle observations of solar reflectances of cloud tops contain information on ice crystal complexity since ice crystal single-scattering properties depend on crystal morphological properties (see section 3.4.1 for more details). As recently shown by Zhang et al. (2020), adding polarization measurements to multi-angle reflectance observations substantially increases the total degrees of freedom to infer ice properties. This is because effects of multiple scattering are minimized in the polarimetric signals leading to rather direct observations of the linear polarization element of the single-scattering phase matrix that depends on ice crystal's microphysical properties. An overview of past studies on ice crystal complexity and shape using multi-angle observations can be found in van Diedenhoven (2018) and a comprehensive study using Multi-angle Imaging SpectroRadiometer (MISR) data combined with Moderate Resolution Imaging Spectroradiometer (MODIS) observations was recently published by Wang et al. (2019). Here, we summarize recent findings of occurrence of complex ice crystals.

Wang et al. (2019) showed using complexity parameter σ_g (as defined by equation (3.2) in section 3.2.2)

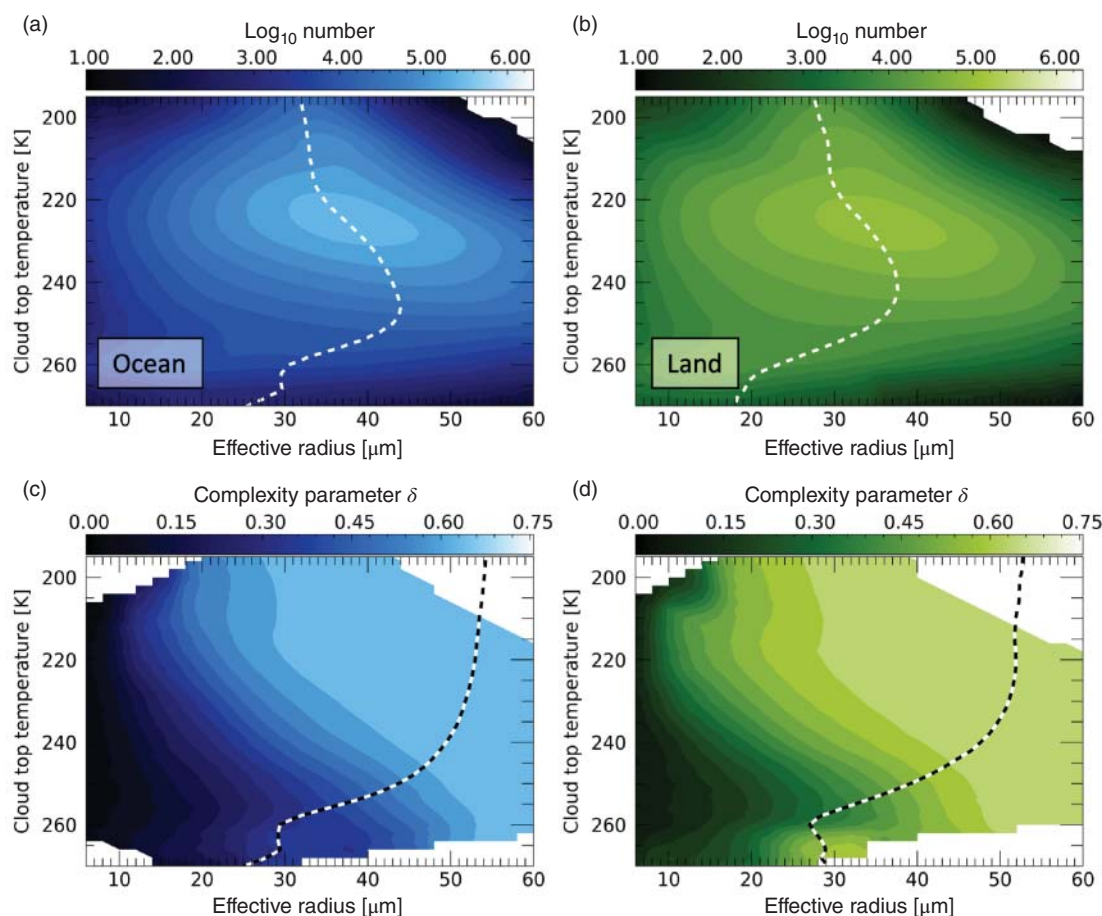


Figure 3.7 Observed number of thick ice clouds with a given combination of cloud top temperature and effective radius over ocean (a) and land (b) and complexity parameter δ as a function of cloud top temperature and effective radius over ocean (c) and land (d). The dashed lines in panels (a) and (b) show the mean effective radius, while the dashed lines in panels (c) and (d) show the mean complexity parameters indicated by the axis labels on top of the color/shade scale bar.

that ice crystal complexity varies weakly with cloud top temperature below 230 K. Furthermore, Wang et al. (2019) found that the occurrence of particles with low complexity is substantially larger for effective radii below 20 μm compared to larger crystals. Similar results were found by van Diedenhoven et al. (2020) who analyzed a year of combined observations of the MODIS spectrometer and POLARization and Directionality of the Earth's Reflectances (POLDER) polarimeter in the A-train satellite constellation. Their approach used hexagonal plates and columns with varying aspect ratios and levels of complexity as proxies for the components of more complex particles. Note that this study used complexity parameter δ (equations (3.1) of section 3.2.2) with a maximum value of 0.7. Only ice clouds with optical thickness above 5 were included. Multi-angle polarimetry allows a very robust filtering of liquid containing cloud tops, leading to a sampling of ice-topped clouds

ranging up to the melting level (van Diedenhoven, Fridlind, et al., 2012). The shortwave infrared bands on MODIS also allow ice effective radius to be inferred. In total, nearly 85 million samples are included in their dataset.

Figure 3.7 shows the number of observed thick ice clouds with a given combination of cloud top temperature and effective radius over ocean and land, in addition to the mean effective radius as a function of cloud top temperature and the variation of complexity parameter δ with cloud top temperature and effective radius. In general, mean effective radii peak for cloud tops at approximately 245 K and are larger over ocean compared to over land. In agreement with the findings of Wang et al. (2019), the complexity parameter δ increases with effective radius, while its variation with cloud top temperature is relatively minimal above 230 K, where mean δ is close to its maximum value of 0.7. For warmer tops, δ generally

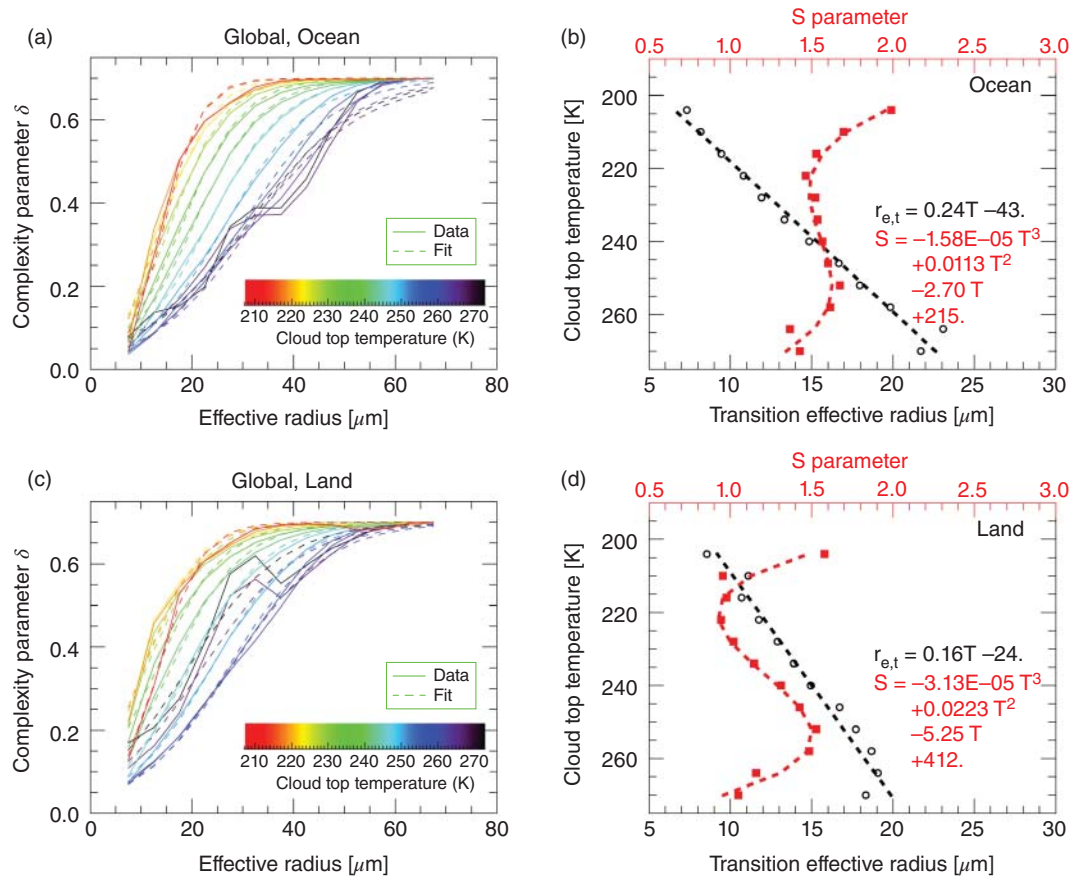


Figure 3.8 Mean complexity parameter δ as a function of effective radius for various cloud top temperature bins as observed (solid lines) over ocean (a) and land (c). Dashed lines show fits using equation (3.7). Panels (b) and (d) show fit parameters $r_{e,t}$ (black, circles) and S (gray/red, squares) from equation (3.7) as a function of cloud top temperature and corresponding polynomial fits.

decreases with cloud top temperature for a given effective radius, also leading to a decrease of mean δ with cloud top temperature. Interestingly, a minimum in δ occurs at around 260 K, which corresponds to the temperature where crystals with extreme aspect ratios are modeled and observed (Jensen et al., 2017; van Diedenhoven et al., 2020).

Similar vertical variation of the complexity parameter shown in Fig. 3.7 is observed independent of the season and latitude (van Diedenhoven et al., 2020) and has also been confirmed by aircraft remote sensing (van Diedenhoven, 2021) in subtropical convective clouds. Previous studies have also shown an apparent trend of decreasing complexity with increasing latitude (e.g., Chepfer et al., 2001; Cole et al., 2014; van Diedenhoven et al., 2020). However, this trend is largely explained by a positive trend of cloud top temperature with latitude. Furthermore, van Diedenhoven (2021) showed significantly higher values of δ for convective cloud tops over ocean that were subsaturated with respect to ice, compared to

supersaturated conditions, which is consistent with the SID-3 observations shown in Fig. 3.6.

Figure 3.8 shows the mean complexity parameter δ as a function of effective radius for various cloud top height bins for clouds over ocean (a) and land (c). A systematic increase of complexity with effective radius is observed, which is consistent with the findings of Wang et al. (2019) discussed above. The rate of increase, however, decreases with increasing temperature. Interestingly, the functional dependence of the complexity parameter on effective radius and its variation with temperature is very similar to the dependence of crystal complexity parameter C (see section 3.2.2) as a function of crystal maximum dimension at various temperatures as derived from in situ observations of the CPI as described by Schmitt et al. (2016). Analogous to the analysis by Schmitt et al. (2016), the relation between complexity parameter δ and effective radius can be well described by

$$\delta(r_e) = 0.7 \left(\frac{\tanh(r_e/r_t - S)}{2} + 0.5 \right), \quad (3.7)$$

where r_t represents the transition effective radius and S determines the slope. Fits of equation (3.7) to observations over ocean and land at various cloud top temperatures are shown in Figures 3.8a and 3.8c. The variation of δ with effective radius is generally well described by equation (3.7), except for the cloud tops warmer than 260 K. The cause of the different behavior for these very warm ice clouds is not known, although we note that the sampling is relatively sparse for these cloud tops. Consistent with the analysis of Schmitt et al. (2016), Figures 3.8b and 3.8d show that the transition size is a linear function of cloud top temperature, for which the least squares fit parameters are shown in the figure. Although Schmitt et al. (2016) remark that no significant trends were found in parameter S of their implementation of equation 3.7, an oscillation in S with cloud top temperature is seen in Figure 3.8d that can be well described by a third-order polynomial.

The transition effective radius may be interpreted as the size above which a transition to mostly complex particles occur. Figure 3.8 suggests that r_t approximately corresponds to the effective radius above which the complexity parameter δ is greater than about 0.2. A plausible explanation for the decrease of r_t with decreasing temperature is the increased lifetime of these ice crystals, which could be caused by slower growth and sublimation rates and slower sedimentation of small crystals that are more typical of colder temperatures. Woods et al. (2018) estimated that cirrus ice crystals in the tropical tropopause layer (TTL), with mean diameters typically below 30 μm , will fall at a rate of only 2 km per day, increasing the likelihood of these crystals to be exposed to greater variations of environmental conditions leading to increased complexity. Furthermore, at colder temperatures subsaturated conditions may be more prevalent leading to more complexity on average (van Diedenhoven, 2021, see also Fig. 3.6).

A limitation of the space-borne remote sensing approaches discussed above is that the observations represent ice crystal properties at the tops of thick ice clouds, which do not necessarily reflect the temperature dependence of crystal properties within deep clouds, or the properties of thinner cirrus clouds. Furthermore, since these remote sensing approaches are based on optical complexity metrics as discussed in section 3.2.2, which represent several physical crystal complexities across multiple scales, the actual nature of the crystal complexities cannot be deduced directly from these observations. It should be also noted that there is a tendency for the remote sensing techniques to yield the maximum-allowed complexity parameter for most observations (e.g., Hioki et al., 2016; van Diedenhoven et al., 2020). This is likely a consequence of the asymptotic behavior of simulated phase matrices at large complexity parameters and may suggest that the complexity parameterizations in these

simulations are not sufficiently representative of highly complex crystals in natural clouds.

Besides observations of multi-angle solar reflectances, the polarization Light Detection and Ranging (lidar) technique is widely used to investigate the microphysical properties of cirrus clouds. The lidar depolarization ratio is used as an indicator of particle non-sphericity since the linear depolarization ratio of non-spherical scatterers can significantly differ from zero. Furthermore, it is believed that the magnitude of the linear depolarization ratio can offer some information on ice crystal morphology. Global CALIPSO-CALIOP statistics show a yearly averaged ice cloud depolarization ratio around 0.34–0.37, with a trend of lidar depolarization (1) increasing with increasing cloud altitude or (2) decreasing temperature and (3) decreasing with latitude (Baum et al., 2011; Okamoto et al., 2020; Sassen & Zhu, 2009; Sassen et al., 2012). Ray-tracing calculations have shown that different randomly oriented pristine ice crystal habits generate different backscattering depolarization ratios (Takano & Liou, 1995), whereas T-matrix calculations and laboratory studies have shown that the linear depolarization ratio has a strong size dependence for small size parameters ($x < 30$) (Mishchenko & Sassen, 1998; Schnaiter et al., 2012), which might explain the maximum depolarization values observed in contrail cirrus (Freudenthaler et al., 1996). In a similar manner, it has been suggested that crystal complexity can lead to changes in the linear depolarization ratio. Theoretical studies with distorted hexagonal columns have shown that linear depolarization ratio has a nonlinear dependency with the distortion parameter (Borovoi et al., 2015). Simulations with complex crystals tend to yield to a better agreement with annually averaged CALIOP data (Baum et al., 2011). Due to the complicated relationship between crystal morphology and the linear depolarization ratio as well as the limitations to simulate the scattering properties of complex ice crystals for the exact backward direction observed by lidars (Borovoi et al., 2014), the quantitative interpretation of depolarization ratios with respect to the complexity metrics discussed in section 3.2.2 remains uncertain. An additional limitation of lidar depolarization measurements is their sensitivity to oriented crystals. Even if a tilt to the lidar is applied, as is the case for CALIOP, the presence of a small fraction of oriented crystals can substantially reduce the depolarization ratio, further complicating the interpretation of the signal (Okamoto et al., 2020).

3.3.4. Synthesis of Ice Crystal Complexity Observations

The origin of ice crystal complexity in natural clouds is not yet well understood. However, some general trends are

observed: (1) both in situ and remote sensing observations (Figs. 3.6 and 3.7) have shown that complexity parameters increase with decreasing temperature, and that (2) higher complexity parameters are observed in subsaturated compared to supersaturated conditions (Fig. 3.6 and van Diedenhoven (2021)). Furthermore, (3) remote sensing observations indicate that complexity parameters increase with increasing effective radius (Fig. 3.7). On the other hand, ice crystals tend to be smaller at lower temperatures so the complexity is, for a given radius, larger for lower temperatures. Laboratory studies have shown that growing ice crystals at higher temperatures would promote complexity through faster crystal growth rates. This can explain the observed increase in complexity parameter with increasing crystal effective radius but cannot explain the increased complexity at lower temperatures.

Increased complexity at lower temperatures might be promoted through sublimation and regrowth cycles in long-persisting cirrus layers near the TTL. Both CSEM and laboratory studies have shown that repeated growth and sublimation cycles can increase the complexity parameters. Sublimation and regrowth is also found to contribute to formation of air pockets in laboratory studies (see section 3.3.1). It is evident that more work is needed to understand the detailed morphological properties of the highest lying cold cirrus ice particles, especially since often they are the first condensed matter encountered by solar light.

3.4. LIGHT SCATTERING BY COMPLEX CRYSTALS

3.4.1. Computer Simulation of Angular Light Scattering by Ice Crystals

Computer simulations are an important tool for gaining fundamental knowledge of scattering and absorption properties of ice crystals, and much research effort has been invested toward this direction in recent decades. Due to their non-sphericity, Lorenz-Mie theory of light scattering by spherical particles can only serve as a first-order approximation to the problem and is not able to reproduce many of the angular scattering or polarization features of aspherical ice crystals. On the other hand, geometric-optics methods can explain much of the fascinating optical phenomena, such as the 22° and 46° halos associated with some cirrus clouds, which result from refractive rays through the prism angles of 60° and 90°. Conventional geometric-optics methods are applicable to faceted particles with a relatively large size parameter, defined as the ratio of particle size to wavelength.

$$x = 2\pi r/\lambda, \quad (3.8)$$

where r is the radius of the equal-volume-sphere. To compute the light scattering properties, one must generate different crystal shapes using computer techniques. Results for many shapes, such as quasi-spherical, column-type, plate-type, and bullet rosette (as shown in Fig. 3.9), have been presented in the literature (e.g., Macke, Mueller et al., 1996; Yang et al., 2018). The databases by Yang et al. (2013) and Bi & Yang (2017) are widely used and include optical properties for solar and infrared wavelengths for crystals of a large range of sizes and nine different shapes.

The scattering phase matrix (often denoted as $\mathbf{P}(\Theta)$, where Θ is the scattering angle) is a fundamental scattering property of ice crystals, which transforms incident Stokes parameters into scattered Stokes parameters. For an ensemble of randomly oriented ice particles, the scattering phase matrix generally has a block-diagonal form:

$$\begin{pmatrix} I \\ Q \\ U \\ V \end{pmatrix} = \frac{\Omega_{\text{eff}}}{4\pi} \begin{pmatrix} P_{11}(\Theta) & P_{12}(\Theta) & 0 & 0 \\ P_{21}(\Theta) & P_{22}(\Theta) & 0 & 0 \\ 0 & 0 & P_{33}(\Theta) & P_{34}(\Theta) \\ 0 & 0 & -P_{34}(\Theta) & P_{44}(\Theta) \end{pmatrix} \begin{pmatrix} I_0 \\ Q_0 \\ U_0 \\ V_0 \end{pmatrix}, \quad (3.9)$$

where $\Omega_{\text{eff}} = \sigma_{\text{sca}}/R^2$, σ_{sca} is the scattering cross-section, and R is the distance between the particle and the point of observation. The element $\mathbf{P}_{11}(\Theta)$, also called the *phase function*, describes the total intensity of the scattered light as a function of the scattering angle and, therefore, is relevant for radiative transfer calculations. For the two-stream radiative transfer approaches applied in most climate models, this element can be represented by the asymmetry parameter, g , defined as the cosine-weighted integral of $P_{11}(\Theta)$:

$$g = \frac{1}{2} \int_{-1}^1 P_{11}(\Theta) \cos(\Theta) d\cos(\Theta) \quad (3.10)$$

In geometric-optics methods, one applies geometric ray-tracing to account for light ray refractions and (external or internal) reflections. Geometric ray-tracing applies Snell's law and the Fresnel formulas, and can be considered an asymptotic approach that becomes applicable when a locally smooth surface is much larger than the incident wavelength, that is, $x \gg 1$. The hit-and-miss Monte Carlo method was applied by, for example, Takano & Liou (1995), Macke, Mueller et al. (1996), and Yang & Liou (1998a), to trace the photons in complex ice crystals with polarization and absorption.

In addition to refraction and reflection, the contribution from diffraction in the far field, or Fraunhofer diffraction, must be determined in order to compute the phase function correctly. Conventionally, diffraction by ice crystals is computed according to Babinet's principle, which states that the diffraction pattern is determined by

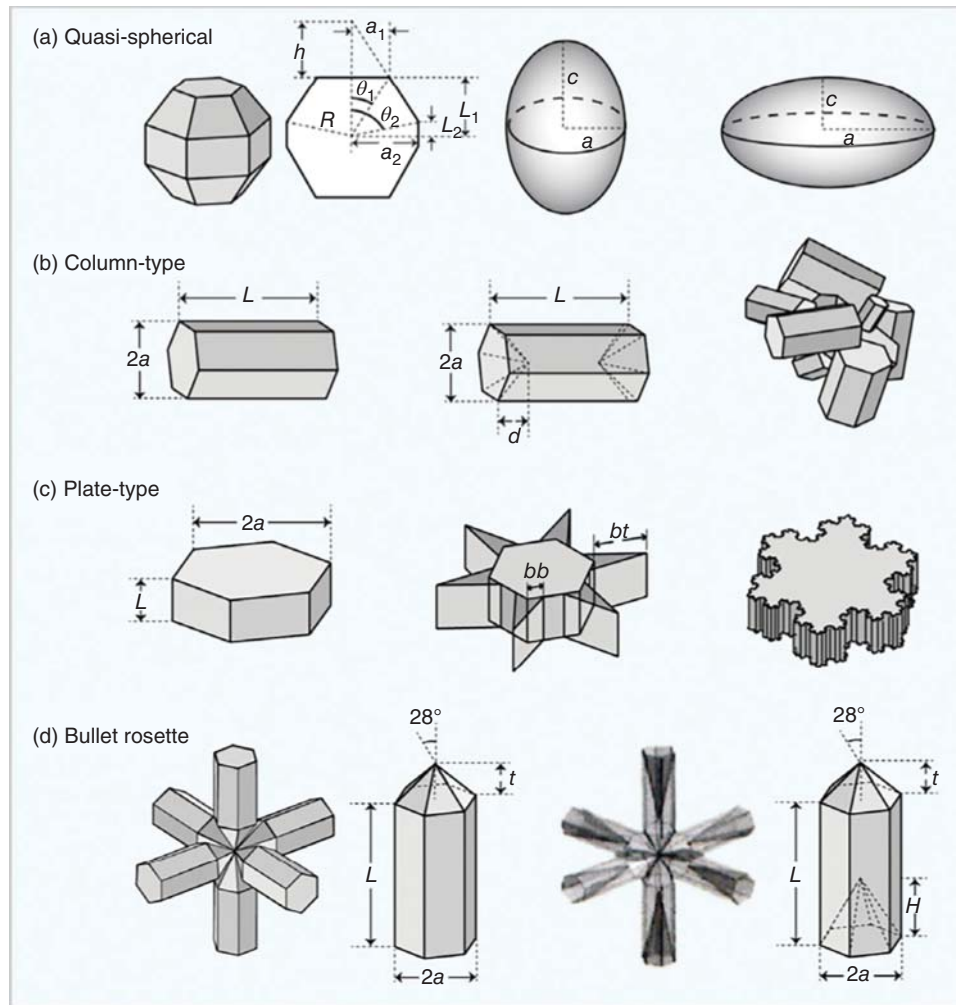


Figure 3.9 Computer-generated shapes for ice crystals. Source: Adapted from Liou & Yang (2016).

its geometric projection on a plane normal to the incident direction. This leads to a contribution to the phase function that is highly peaked in the forward scattering direction. The diffraction asymmetry parameter is generally approximately unity, but decreases for size parameters below about 100. In addition to the application of the Babinet's principle for diffraction computation, Hesse et al. (2012) extended the method to cases of oblique apertures, with good agreement with numerical exact results. The conventional geometric ray-tracing method assumes that the contributions of diffraction and Fresnel rays are equal, and the extinction efficiency is 2 (Bi et al., 2014). Such methods are only applicable to relatively large size parameters above 30–40 (Takano et al., 1992). To overcome these limitations, Yang & Liou (1996b) developed an improved method by mapping the near field to the far field based on the electromagnetic equivalence theorem. This mapping can be realized by either the surface integral equation or the volume integral equation.

The refraction and reflection calculations using geometric ray-tracing by definition do not depend on particle size for non-absorbing wavelengths (e.g., at visible wavelengths). Furthermore, as discussed above, the diffraction contribution is only sensitive to particle size for size parameters below about 100. Hence, for size parameters greater than about 100, the phase matrix and g derived by geometric optics calculations do not depend substantially on particle size for non-absorbing wavelengths, but only on crystal morphology (see Fig. 3.10). Note that morphology itself may depend on size, leading, in turn, to size-dependent scattering properties. At absorbing wavelengths, the refraction and reflection contributions are affected by light absorption, while the diffraction is not. Hence, the relative contribution of diffraction to the total phase function increases with increasing absorption (i.e., decreasing single-scattering albedo (SSA)), leading to an increase of g (Macke, Mueller, et al., 1996). As SSA decreases with particle

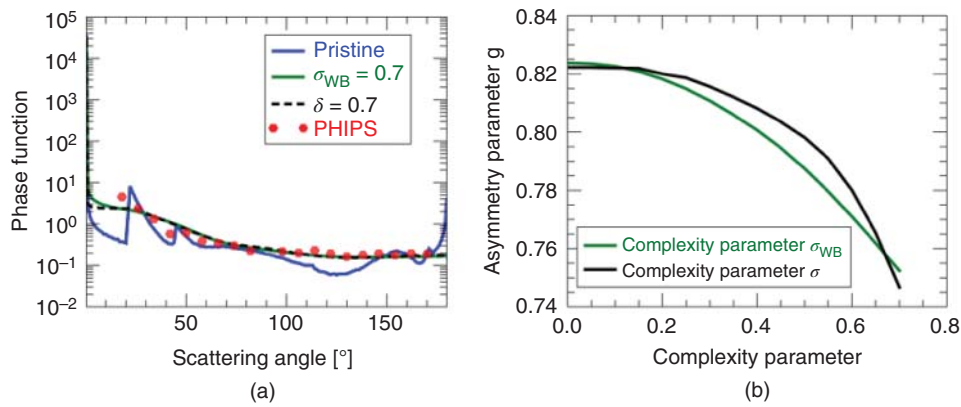


Figure 3.10 Panel (a) shows the phase functions of a hexagonal columnar prism with an aspect ratio of 0.5 (defined as the ratio of crystal basal plane width and prism length) without any complexity (dark gray/blue) and with complexity added using uniform facet tilt (equation (3.1) with $\delta = 0.7$ (black dashed line) and with complexity added using a Weibull distribution (equation (3.3) with $\sigma_{wb} = 0.7$ and $\eta = 0.75$ (gray/green). The gray/red hexagons represent observations of columnar crystals with aspect ratio restricted between 0.4 and 0.6 (defined as the ratio between the width perpendicular to maximum dimension and the maximum dimension) measured with the Particle Habit Imaging and Polar Scattering (PHIPS) probe. Panel (b) shows the decrease of asymmetry parameter with increasing parameter σ_{wb} (gray/green) and δ (black).

size, g increases with particle size at such absorbing wavelengths.

Geometric-optics methods are often applied to faceted particles with smooth surfaces. To account for ice crystal complexity, a TF approach is generally used to mimic the effect of facet roughness by changing the outgoing direction of a traced ray in the ray-tracing process, as discussed in section 3.2.2. This random facet tilt procedure can diminish the halos produced by pristine ice crystals, that is, the peaks in the scattering function at 22° and 46° scattering angle. A typical example is shown in Figure 3.10a, where the phase function of a pristine hexagonal column is compared to that of a column with complexity parameterized by using a uniform facet tilt (equation (3.1) with $\delta = 0.7$ and using a Weibull distribution for the facet tilt (equation (3.3) with $\sigma_{wb} = 0.7$ and $\eta = 0.75$). The two methods to parameterize the optical effects induced by crystal complexity lead to a similarly smooth phase functions in Figure 3.10a. Both parameterizations accurately represent the observed median angular scattering function of columnar crystals in the side and back-scattering angular range. However, there is a significant discrepancy for scattering angles $< 50^\circ$, most likely because the complete randomization of the crystal surfaces in the model diminishes the halo features from less roughened facets that might still be present in the actual particle population. Furthermore, an increase in complexity generally decreases g of the scattering phase function (Macke, Mueller, et al., 1996), as demonstrated in Figure 3.10b.

In addition to crystal facet roughness, the TF approach has also often been used to simulate the optical effects of

other types of crystal complexities, such as internal structures (Hong & Minnis, 2015; Macke, Mishchenko, et al., 1996) and macro-scale complexities (Letu et al., 2016). Here, it has to be emphasized that even though the TF method is widely used, it represents a rather non-physical approach to the light scattering properties of complex ice crystals, and it has not yet proven to be a good proxy for all the different types of complexities, with many having scales around the incident wavelength or smaller (i.e., outside the geometrical optics region) observed in real atmospheric ice crystals (see section 3.2.1).

In addition to geometric-optics methods, large efforts have been invested into the development of numerically accurate methods, such as the T-matrix method (Bi et al., 2013; Draft Johnson, 1988; Mishchenko & Travis, 1998; Waterman, 1971), the discrete-dipole approximation (DDA) (Draine & Flatau, 1994; Purcell & Pennypacker, 1973; Yurkin et al., 2007; Yurkin & Hoekstra, 2011), the finite-difference time domain (FDTD) (Sun et al., 1999; Taove & Umashankar, 1990; Yang & Liou, 1996a), and pseudo-spectral time domain (PSTD) methods (Liu, 1997; Liu et al., 2012). These methods can be used for accurate simulation of optical properties of ice crystals possessing a high degree of morphological complexity. In addition, they can be applied to examine the accuracy of the traditional geometric-optics treatments, for example, of diffraction (Mishchenko & Macke, 1998), and facet roughness (Collier et al., 2016; Riskilä et al., 2021). However, these methods are more suitable for simulations of crystals with relatively small size parameter, that is, for small crystals and/or long wavelengths, because (unlike

geometric optics methods) computation times increase significantly with increasing size parameter.

3.4.2. In situ Observations of Ice Crystal Angular Light Scattering Functions and Ice Cloud Asymmetry Parameter

Direct measurement of the angular distribution of light scattered from ice crystals is important for developing optical particle models, such as those discussed in section 3.4.1, that are used to parameterize cloud optical properties in climate models. The ice crystal angular light scattering function can be measured in situ using nephelometers. There are several types of nephelometers (Barkey et al., 2012), all containing a collimated light source (usually a laser) and a (set of) detector(s), that can be either stationary or moving, measuring the scattered light intensity at desired angles from near-forward scattering to near-backscattering angles. Since it is technically difficult to measure the scattered light down to 0° and 180° , some assumptions for the fraction of scattered intensity outside the measurement range need to be made in order to derive g (Gerber et al., 2000; Xu et al., 2022).

Nephelometer measurements have been performed since the 1960s. The early measurements were conducted in the laboratory for artificially generated ice clouds (Dugin et al., 1977; Human, 1970; Rimmer & Saunders, 1997; Sassen & Liou, 1979; Sasaki et al., 1998). These studies reported poor agreement between experimental and theoretical angular scattering functions when assuming spherical particles or simple habits, such as infinitely long cylinders or pristine hexagonal particles. Since the 1990s, in situ measurements of the angular scattering function (and g) have been available from airborne polar nephelometers (e.g., Gayet et al., 1998; Garrett et al., 2001, 2003). In this section, we present angular scattering function measurements of a single oriented ice crystal and give an overview of in situ observations of g in different geographical locations.

Angular Light Scattering of Individual Oriented Ice Crystals

Attempts to experimentally characterize the angular scattering from single ice crystals having well-defined orientation have been quite limited. Yet, testing ray-tracing or other optical models against single oriented ice crystals would bring valuable information on how crystal complexity is affecting light scattering in detail. A first step in this direction was undertaken by Shcherbakov et al. (2006), who connected a polar nephelometer in tandem to a cloud particle imager. With this setup they measured angular light scattering functions and habits for individual ice crystals from diamond dust events at the South Pole. Although the two measurements were

not performed on exactly the same individual crystals, the measurement setup ensured that the two instruments sampled the same crystal population in a statistical sense. They report highly variable angular light scattering functions with distinct peaks that are attributed to quasi-specular reflections from crystal facets of oriented ice crystals. Ray-tracing analysis with TF complexity metrics, for example, assuming Weibull distributed surface height gradients (equation 3.3), revealed that roughness parameters corresponding to deeply rough surfaces are necessary to reproduce the observed features in the angular scattering functions. While broad quasi-specular reflections could be reproduced by this approach, significant differences between modeled and measured angular scattering functions were observed for scattering angles between 125° and 160° . These discrepancies at backward angles were attributed by Shcherbakov et al. (2006) to shortcomings of the geometric-optics approximation and, in particular, the neglect of diffraction effects on individual elements of the surface roughness texture in the ray-tracing approach.

The Particle Habit and Polar Scattering (PHIPS) probe is an airborne single particle instrument that was developed to fill the knowledge gap in understanding the fundamental light scattering properties of individual atmospheric ice particles. Basically, PHIPS measures both the ice particle habit and its orientation, as well as the corresponding angular light scattering function for the *same* crystal at the *same* orientation. This is achieved by combining a stereo-microscopic imager with a polar nephelometer in a single instrument (Abdelmonem et al., 2016; Schnaiter et al., 2018). With PHIPS it is now possible to reconstruct the habit and orientation of observed individual ice crystals in order to test and refine optical models by comparing their light scattering results with corresponding measurements. In this way, existing optical models can be tested for their performance in reproducing ice crystal light scattering characteristics for the different morphological complexity types and ranges presented in section 3.2.

Figure 3.11a shows an example of a columnar ice crystal captured by PHIPS during the SOCRATES project over the Southern Ocean. The 3-D reconstruction of the crystal revealed a size of $40\mu\text{m}$ and $86\mu\text{m}$ for the a -axis and c -axis lengths, respectively. The optical engineering software FRED (Photon Engineering, Tucson, AZ) was used to perform ray-tracing calculations for this crystal in order to simulate the PHIPS light scattering measurement. Ray-tracing calculations were conducted for smooth facets as well as for roughened surfaces by activating either tilted-surface Weibull statistics or the ABg surface roughness diffraction model on individual facets of the crystal (see section 3.2.2 for details). While the hemispheric irradiation map of scattered light shows

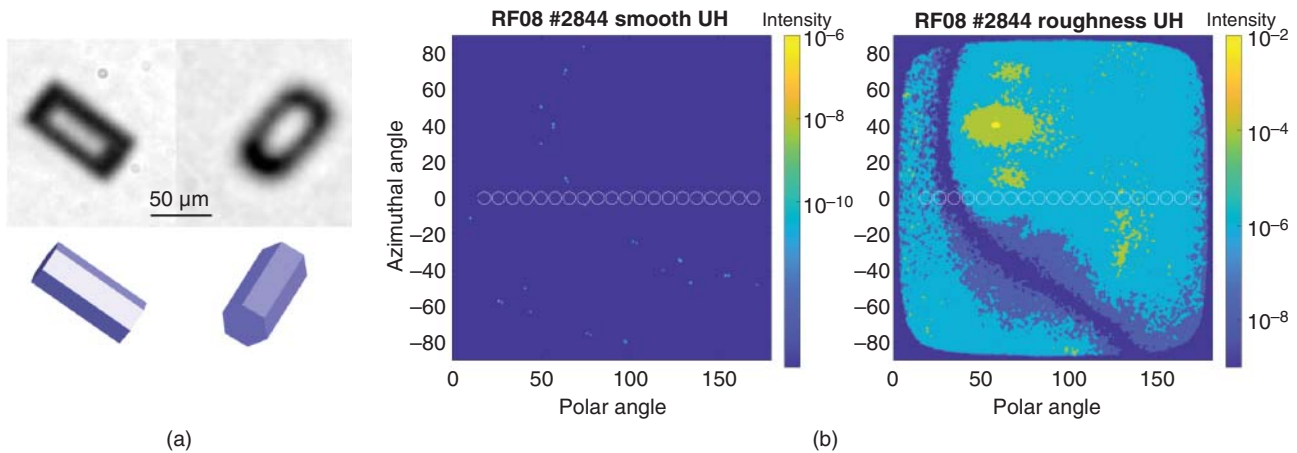


Figure 3.11 Columnar ice crystal (crystal number 2844) captured by PHIPS during the SOCRATES project over the Southern Ocean (a). The spatial light scattering of the single oriented crystal was simulated assuming smooth facets (smooth) and facets with added nanoscale surface roughness (roughness). Panel (b) shows the corresponding irradiation maps of light scattered in the upper hemisphere (UH), where the detectors are located. The color scale illustrates the scattering intensity so that lighter shade/color corresponds to a higher intensity and darker shade/color to a lower intensity. The white circles overlaid in the irradiation maps illustrate the solid angles of the nephelometer detectors. (a) Stereo-microscopic image of a columnar ice crystal and its 3-D reconstruction. (b) Hemispheric irradiation maps.

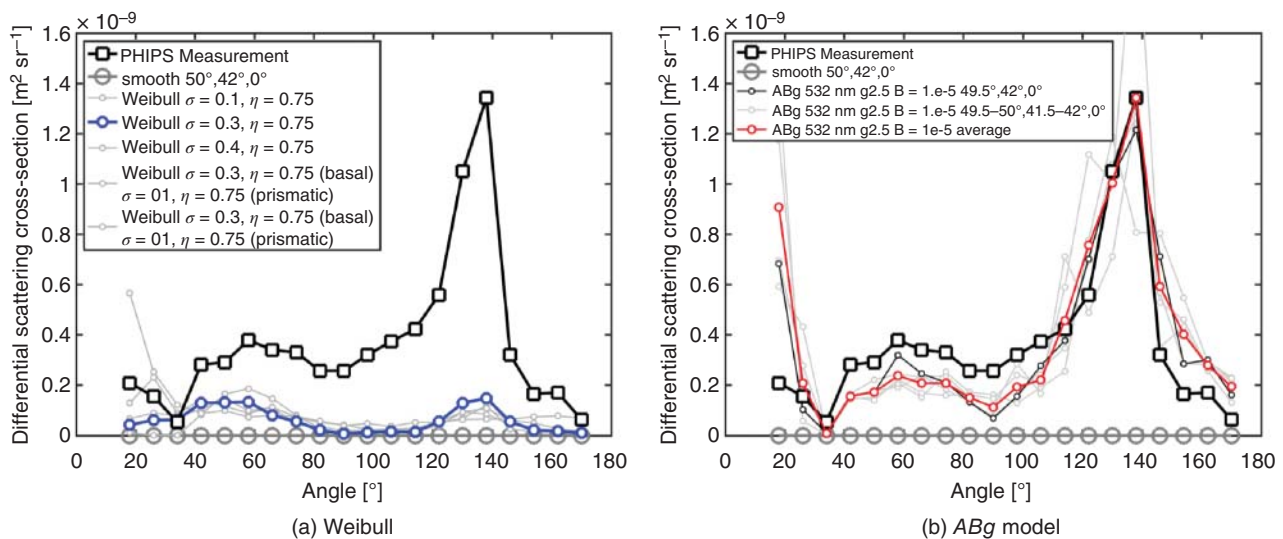


Figure 3.12 Measured and modeled differential scattering cross-sections of a columnar ice crystal displayed in Figure 3.11. Measurements are represented with black squares. Round symbols show calculations assuming rough surfaces where surface roughness was simulated using TF method and Weibull statistics (a) and the ABg model (b), respectively.

distinct ray spots in the case of smooth crystal facets, the scattered radiation is more evenly distributed across the hemisphere when the basal facets of the crystal were assumed to be rough (Fig. 3.11b).

The angular scattering function measured for this crystal by PHIPS, displayed in Figure 3.12, shows a distinct maximum in the 120° to 150° angular range, with

a peak in the 138° channel, a less-marked and broad maximum in the 40° to 80° angular range, followed by a shallow minimum around 90° , a sharp minimum at 34° , and a significant non-zero scattering cross-section for the other channels. Interestingly, the ray-tracing result for the crystal with smooth facets does not predict scattered radiation in any of the PHIPS detection channels. Only

if surface roughness is assumed for the basal facets of the crystal, do the ray-tracing calculations predict an angular light scattering profile that resembles the measurement. The measured angular scattering function of this crystal (at this specific orientation) can, therefore, be solely explained by surface roughness on the basal facets, and the two optical complexity metrics introduced in section 3.2.2 can be tested for this case. While the TF approach with Weibull statistics equation (3.3) follows the general trend of the measured scattering function, it shows significant deviations in feature position and shape and, in particular, the strength of predicted light scattering (Fig. 3.12a). Yet, the ABg roughness diffraction model equation (3.5) mimics the measurement quite well (Fig. 3.12b). This is true not only for the position and shape of the observed features but also for the strength of the predicted light scattering, which indicates that, in a case of this specific crystal, a physical (diffraction) based model gives better results than a TF approximation that ignores diffraction on the sub-wavelength scale features of the surface. It is clear that a final assessment of the performance of these two approaches (or any other approach to simulate the optical effect of crystal complexity) cannot be made based on one specific case. Rather, this example emphasizes the value of measuring and analyzing angular light scattering functions of individual oriented ice crystals.

Ice Cloud Asymmetry Parameter Derived from In situ Measurements

Here, we report observations of g from three different in situ instruments: the polar nephelometer (PN), the Cloud Integrating Nephelometer (CIN), and the PHIPS probe. All three instruments measure light scattering of cloud particles approximately in the size range from a few micrometers up to 1mm in diameter and in an angular range from near-forward direction to near-backward direction. Different methods are used to derive g from the measurements of scattered intensities. To derive g from PN (CIN) measurements, it is assumed that the fraction (f) of energy scattering into angles smaller than 15° (10°) is constant. For PN, it is assumed that $f = 0.56$ regardless of the cloud composition, whereas for CIN f varies between 0.52 and 0.57 (Gerber et al., 2000). It is estimated that the absolute error in g derived from PN measurements is ± 0.04 , and the relative error for CIN is 3%. For PHIPS, g was retrieved by fitting an optical particle model from the database of Yang et al. (2013) to the measurements. The best fit was achieved using model particles composed of severely roughened column aggregates. Recently, Xu et al. (2022) introduced a method for deriving the asymmetry parameter from a polar nephelometer, without relying on specific light scattering models.

Table 3.2 summarizes the retrieved values for g and also values for simultaneously retrieved extinction coefficient, β . Values given for g and β are averages for one airborne measurement campaign, except in the case of PHIPS, where data are averaged over several campaigns. In general, g values below 0.79 are observed, which is less than expected for pristine hexagonal crystals (e.g., Fig. 3.10b). The apparently systematic difference in g between the different nephelometers can be partly explained through the uncertainty in the methods used to retrieve g , as discussed above. Additionally, in situ measurements cover a smaller spatial and temporal scale compared to, for example, satellite observations, and, therefore, the magnitude of g also depends on the sampled cloud conditions. Also, no inter-comparison studies have been reported between the different nephelometers, which would help to evaluate the differences.

Figure 3.13 shows g as a function of in-cloud temperature and RH_{ice} measured with the PN in three airborne campaigns. These campaigns covered different cirrus types and origins: in the CIRCLE campaign most of the sampled cirrus clouds were either of convective outflows or synoptic origin whereas in the interhemispheric differences in cirrus properties from anthropogenic emissions (INCA) campaigns mostly synoptic or wave cirrus with lower vertical velocities (from 1 to 35 cm s^{-1}) were measured. Figure 3.13 shows that g decreases slightly from 0.765 to 0.755 with decreasing temperature in the INCA campaigns, presumably as a result of change in ice crystal size and morphology. In the CIRCLE campaign, g increased toward colder temperatures, which might be explained by the presence of high concentrations of quasi spherical or sublimating small ice crystals near the cloud top of convective anvil cirrus, which have been shown in some occasions to lead to an increase in g (Gayet et al., 2012; Järvinen et al., 2016). Small “pristine” plates were also observed close to the cloud top of synoptic cirrus, resulting in reduced side scattering and enhanced forward scattering (i.e., higher g). Panel (b) in Fig. 3.13 shows the same set of data for INCA campaigns but now as a function of RH_{ice} . Only a slight increase in g with increasing RH is observed toward RH values around 130%.

The observed low g between 0.75 and 0.79 for clouds with temperature ranging from 235 K to 210 K support the findings discussed in previous section. Both theoretical (see section 3.4.1) and laboratory studies (Järvinen et al., 2016; Schnaiter et al., 2016; Ulanowski et al., 2006) have shown that g decreases with increasing crystal complexity. It has been proposed that crystal complexity is the main driver of ice crystals’ angular scattering behavior (and thus g) in the solar wavelengths (Järvinen et al., 2018a; Schnaiter et al., 2016) so that the underlying ice crystal habit becomes less important in an optical sense. This would partly explain why

Table 3.2 Values of asymmetry parameter (g) and extinction coefficient (β) estimated from previous in situ measurements in ice clouds.

Cloud type Instrument	g	β (km ⁻¹)	References
ML cirrus (Cirrus 98') PN (800 nm)	0.79 [0.78–0.79]	0.86 [0.5–1.5]	Jourdan et al. (2003)
NH cirrus (INCA 2000) PN (804 nm)	0.767 [0.76–0.77]	0.63 [0.29–1.3]	Gayet et al. (2004)
SH cirrus (INCA 2000) PN (800 nm)	0.767 [0.76–0.77]	0.49 [0.22–0.97]	Shcherbakov et al. (2005)
ML cirrus (CIRCLE-2 2007) PN (804 nm)	0.778 [0.77–0.78]	0.4 [0.2–1]	Mioche et al. (2010)
Polluted cirrus (CONCERT 2008,2011) PN (804 nm)	0.77 [0.76–0.79]	0.21 [0.05–0.6]	Chauvigné et al. (2018)
Several cloud types PHIPS (532 nm)	0.75		Järvinen et al. (2018a)
Arctic ice clouds CIN (635 nm)	0.74±0.03	~0–30	Gerber et al. (2000) Garrett et al. (2001)
Florida anvil CIN (635 nm)	0.75±0.01		Garrett et al. (2003)

Note: ML = Midlatitude, NH = Northern Hemisphere, and SH = Southern Hemisphere.

similar g is measured in different types of clouds with different origin (liquid-origin or in situ), although it is known that the ice crystals habits can be very different. However, the limitation of in situ measurements is their spatial restriction, whereas a more global picture of g can be gained through space-borne remote sensing observations.

3.4.3. Ice Cloud Asymmetry Parameter Inferred from Space-Borne Remote Sensing Observations

Cloud optical thickness and effective radius inferred from a bi-spectral method using visible and shortwave infrared reflectances are substantially sensitive to g of the assumed optical model in the retrieval algorithm. If the true optical thickness and asymmetry parameter at visible wavelengths are τ_{true} and g_{true} , and the assumed asymmetry parameter is g_{mod} , the relative bias in the retrieved optical thickness τ_{retr} can be approximated by

$$\tau_{\text{retr}} \approx \tau_{\text{true}} \frac{1 - g_{\text{true}}}{1 - g_{\text{mod}}}, \quad (3.11)$$

while the relative bias in retrieved effective radius is approximately the inverse of the optical thickness bias (Stephens et al., 2001; van Diedenhoven, Cairns, et al., 2012; van Diedenhoven, Cairns, et al., 2020). Hence,

reducing uncertainties in the magnitude of g at visible wavelengths is crucial to reducing uncertainties in retrieved ice cloud optical thickness and effective radius. For a recent review of ice optical models used for such retrievals, we refer to Yang et al. (2018).

As discussed by Yang et al. (2018), equation (3.11) can be used to estimate g at the shortwave if a collocated retrieval of optical thickness and/or effective radius is available from another technique that is less sensitive to the ice particle scattering properties. One of the earliest examples of such an approach was presented by Stephens et al. (1990), who used a combination of airborne visible and thermal infrared (TIR) measurements over cirrus to conclude that g close to 0.7 is consistent with the data. More recently, Holz et al. (2016) used optical thickness inferred from passive thermal infrared (TIR) as a reference to evaluate the optical model for the latest MODIS ice cloud bi-spectral retrievals. That work showed that, for severely roughened aggregates of columns, a value of g of about 0.75, on average, agrees with the TIR retrievals. Furthermore, they showed this ice model is also consistent with CALIOP lidar observations. Note that both TIR and lidar retrievals of optical thickness are applicable to clouds with optical thickness less than about 3–5. Similar agreement between TIR and visible cloud optical thickness retrievals is obtained using a two habit model

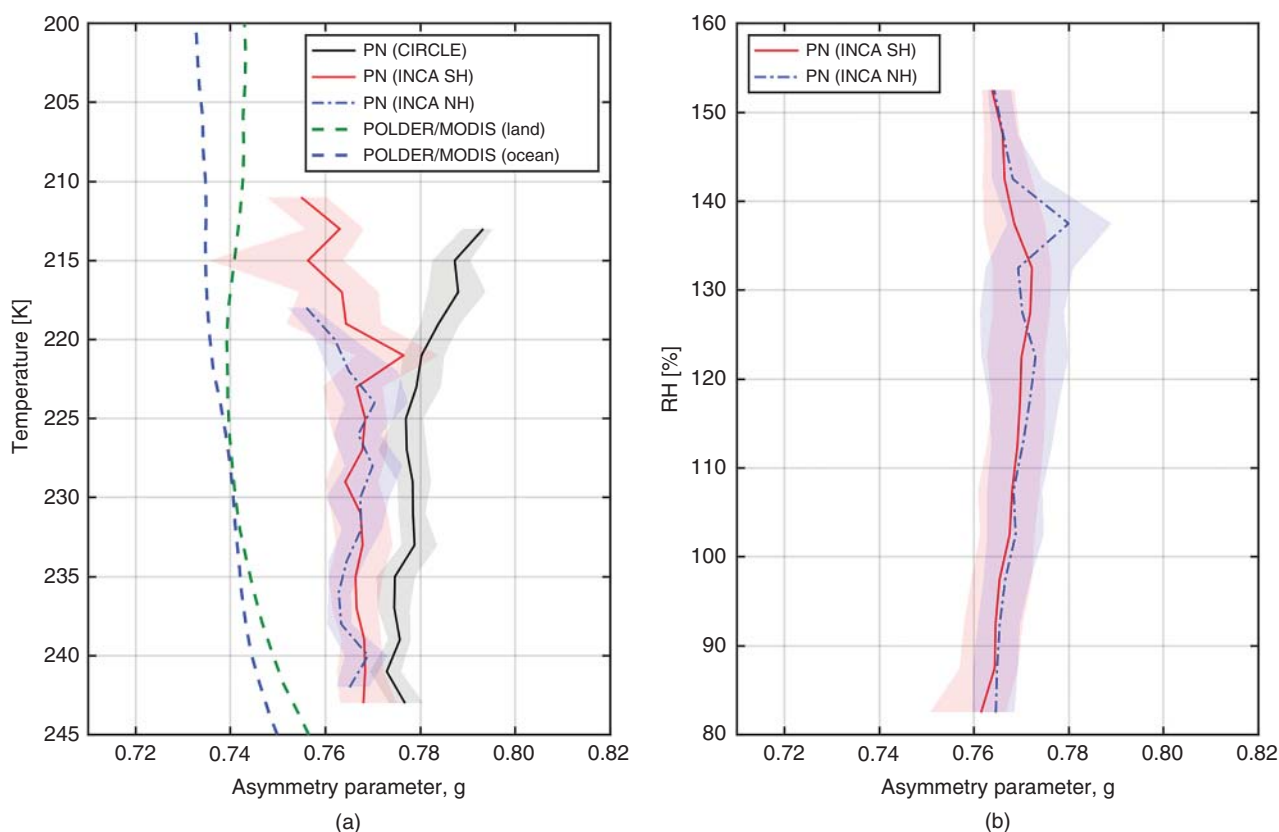


Figure 3.13 Asymmetry parameter (g) as a function of temperature (a) and relative humidity (RH) with respect to ice (b). Measurements were performed with the Polar Nephelometer (PN) probe in three airborne campaigns: CIRCLE (black solid line), INCA in Southern Hemisphere (SH, gray/red solid line), and INCA in Northern Hemisphere (NH, gray/blue dash-dotted line). RH data were not available for CIRCLE campaign. Curves represent median values and shaded areas the 25th and 75th percentile. The dashed lines in panel (a) illustrate the mean asymmetry parameter observations retrieved from POLDER and MODIS observations shown in Figure 3.14.

that also has a g near 0.75 (Liu et al., 2014). However, the assumption of isothermal cloud layers and the neglect of scattering effects may lead to biases in operational TIR retrievals (Saito et al., 2020), while lidar-derived optical thicknesses are affected by uncertainties in lidar ratios (Yorks et al., 2011).

Asymmetry parameters can also be estimated indirectly by inferring crystal morphology from lidar depolarization or multi-angular measurements, as discussed in section 3.3, and using g associated with that shape as the retrieved value. This approach applied to multi-angle polarimetry was evaluated with simulated measurements based on several smooth and roughened ice crystal habits by van Diedenhoven, Cairns, et al. (2012), who conclude that g can be retrieved within 5% for individual measurements.

Several studies showed that ice models with g near 0.75, such as the severely roughened aggregates of columns or the roughened two habit model, lead to a general good agreement with global satellite measurements (Liu

et al., 2014; Letu et al., 2016; Yang et al., 2013; Yang et al., 2018). Similarly, the crystal shape and complexity parameter δ retrieved from global POLDER observations of thick ice clouds as discussed in section 3.3 and shown in Figure 3.7 can be used to infer g , of which mean values as a function of cloud top temperature and effective radius are shown in Figure 3.14. As discussed by van Diedenhoven et al. (2020), the globally averaged g agrees with the value of 0.75 inferred by other studies, but substantial variation is seen. Specifically, mean g is observed to increase with increasing cloud top temperature, especially for cloud top temperatures above about 240 K (Fig. 3.14). Furthermore, g is found to decrease with increasing ice effective radius. This variation of g is mainly affected by the variation of crystal complexity with cloud top temperature and effective radius, as shown in Figure 3.7. The value of mean g around 0.75 and its weak dependence on temperature for cloud tops colder than 240 K is generally consistent with in situ observations discussed in section 3.4.2. Furthermore, the

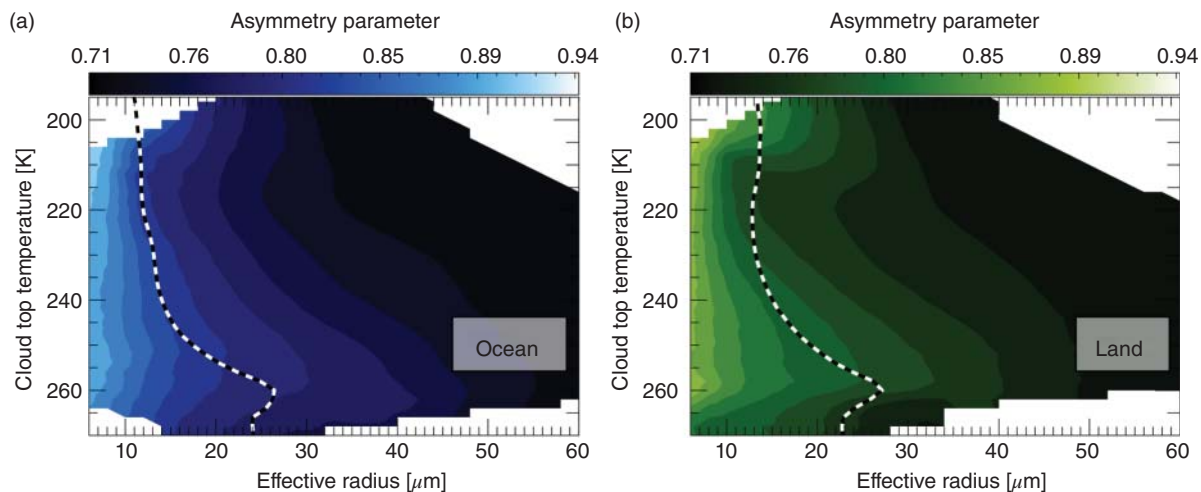


Figure 3.14 Observed global average of cloud top ice asymmetry parameters as a function of cloud top temperature and effective radius for thick ice clouds over ocean (a) and land (b). The dashed line shows the mean asymmetry parameters as a function of cloud top temperature indicated by the axis labels shown on top of the color/shade scale bar.

increase of g with increasing temperature above 240 K is consistent with the parameterization of Baran (2012).

3.5. THE IMPACT OF CRYSTAL COMPLEXITY ON ICE CLOUD RADIATIVE EFFECT

Ice cloud CRE, and radiation in general, is driven by three ice crystal single-scattering optical properties: the extinction cross-section (σ_{ext}), SSA, and g . For a given wavelength, σ_{ext} and SSA are mostly dependent on size, while g is also influenced by ice crystal complexity as discussed above. Other factors affecting CRE – independent from ice crystal morphological properties – are solar zenith angle, cloud height, surface temperature, and surface reflectivity. Because radiative transfer takes place in a volume, SSA and g need to be integrated over the size distribution of ice crystals weighted by extinction or scattering cross-sections (e.g., Twomey, 1977) to get the bulk optical properties. Similarly, the bulk extinction coefficient is computed by integrating σ_{ext} over the particle size distribution.

In radiative transfer, a frequently used quantity is the mass extinction coefficient, defined as the extinction coefficient (denoted here as β_{ext}) divided by the mass density of ice crystals (IWC). The resulting mass extinction coefficient, which we denote here as β_m , therefore has dimensions area/mass. Also of interest is the dimensionless total cloud optical thickness (or “optical depth”), obtained from these quantities as the profile-integrated product of IWC and β_m .

Ice cloud CRE at TOA is primarily dependent on the cloud optical thickness. Crystal complexity affects foremost g , which creates a source of uncertainty in the

estimations of ice cloud CRE for a given cloud optical thickness and height both in climate models and remote sensing techniques. For example, in remote sensing, the scaled optical thickness (a product of optical thickness and $(1 - g)$, equation (3.11) determines the radiance used for retrievals. Furthermore, while climate models generally predict the vertical variation of IWC and sometimes crystal size, they generally do not constrain crystal morphology or complexity, which is therefore a source of uncertainty when relating the models’ predictions to CRE. Previous estimates show that uncertainties in g need to be generally less than about 5% to determine the top of atmosphere fluxes in atmospheres overcast by ice cloud to within 5%, but these uncertainty limits depend on many factors (Vogelmann & Ackerman, 1995).

In this section, we first provide a general discussion on the estimation of ice cloud CRE, after which uncertainties in CRE related to ice crystal complexity are discussed. A more general discussion of cloud-radiative effects from a remote sensing perspective is provided in Chapter 4: Cloud-Radiation Interactions and Cloud-Climate Feedbacks.

3.5.1. Estimating Ice Cloud CRE

There are several different ways to estimate the radiative effect of ice clouds. This effect can be estimated (1) directly from observations of radiances or irradiances (Ramanathan et al., 1989), (2) using remotely retrieved or in situ observations of ice cloud optical properties (e.g., Campbell et al., 2016; Lolli, Campbell, et al., 2017; Campbell et al., 2021; Kato et al., 2008; L’Ecuyer et al., 2008), or (3) using modeled cloud properties

(e.g., Soden et al., 2004). The first approach is based on direct observations of radiation. However, it is sometimes difficult to separate cloud effects from other radiative effects that might accompany a cloud, such as variations in water vapor and temperature (Loeb et al., 2018; Sohn et al., 2010). The second approach is subject to retrieval errors, although (fortunately) when cloud properties are derived from observed radiances at discrete wavelengths observed by satellite, retrieval errors are partially canceled in irradiance computations (Loeb et al., 2018). The third approach is used by all climate models. These estimates are affected by ice crystal morphology and complexity in numerous ways: not only via optical properties of individual ice particles, but also via the occurrence and lifetime of cirrus clouds (Gasparini et al., 2019; Hartmann et al., 2018).

In the first approach discussed above, the CRE is defined as the irradiance difference between all-sky conditions in which the cloud fraction can vary from 0 to 1 (hereinafter all-sky) $F_{all,y}^{TOA}$ and clear-sky conditions (i.e., no cloud is present, hereinafter clear-sky) $F_{clr,y}^{TOA}$,

$$CRE_y^{TOA} = F_{all,y}^{TOA}(x_{all}) - F_{clr,y}^{TOA}(x_{clr}), \quad (3.12)$$

where the subscript y indicates either SW or LW, x_{all} is atmospheric and surface variables under all-sky conditions (e.g., specific humidity, temperature profiles, and aerosols) and x_{clr} is those under clear-sky conditions. Generally, specific humidity is larger when clouds are present compared to clear-sky conditions. Similar CREs can be defined at the surface or net atmosphere (net TOA minus net surface irradiance). To a good approximation, TOA irradiance under all-sky conditions is a linear combination of cloudy-sky (i.e., overcast) irradiance and clear-sky irradiance weighed by their area fraction,

$$F_{all,y}^{TOA}(x_{all}) = f F_{cld,y}^{TOA}(x_{cld}) + (1 - f) F_{clr,y}^{TOA}(x_{clr}), \quad (3.13)$$

where f is the cloud fraction and x_{cld} is the atmospheric state under overcast conditions. For approaches (2) and (3) discussed above, CRE can be computed by removing clouds while other meteorological conditions stay the same to isolate the effects of clouds on radiation. Therefore, the second term on the right side of equation (3.13) is equivalent to $F_{clr,y}^{TOA}(x_{all})$.

Under daytime conditions, ice clouds generally increase reflected SW irradiance at the TOA and reduce outgoing LW irradiance, relative to clear-sky conditions; these have opposing effects on the ice cloud CRE. The magnitude and sign of the ice cloud CRE therefore depend on numerous environmental conditions, including the underlying surface albedo, and physical characteristics of the cloud (e.g., altitude, temperature, particle size and morphology, and ice-water path/optical depth) (Campbell et al., 2016; Min et al., 2010). In contrast, in the absence of incoming

solar radiation (i.e., at night), all clouds warm the planet by trapping the outgoing thermal radiation.

The Magnitude of CRE as a Function of Cloud Optical Thickness

The CRE defined by equation (3.12) is also used to derive the CRE observationally. For example, TOA irradiances are derived from Clouds and the Earth's Radiant Energy System (CERES) observations of broadband radiances. An overview of the CERES project is given by Wielicki et al. (1996). An empirical relationship is used to convert the radiance to irradiance (Loeb et al., 2005; Su et al., 2015). The relationship depends on scene type of the radiance measured in a CERES footprint. The scene type includes cloud fraction over the footprint, water phase, optical thickness, top height of clouds within the footprint, and surface type. CERES instruments are currently on NASA's Terra and Aqua, Suomi NPP, and NOAA-20 satellites. For Terra and Aqua satellites, radiances measured by MODIS are used to determine the scene type. The theoretical basis of how the irradiance is derived from radiance observations from CERES instruments is given by Kato et al. (2020).

Figure 3.15 shows TOA CRE derived from CERES observations over the tropics (15°N to 15°S) as a function of cloud optical thickness and cloud top height. As expected, cirrus TOA SW CRE and LW CRE appear with opposing signs, and magnitudes that increase with cloud optical thickness. Moreover, the magnitude of SW CRE for a given optical thickness is seen to increase with cloud top height; this is attributable to a reduction in absorption by underlying water vapor when clouds are at higher altitude. In addition, LW CRE for a given cloud optical thickness is seen to increase with cloud top height, attributable to an increased difference between the effective cloud temperature and the temperature of the underlying surface. Progressing from thin to thick, the figure shows that the daytime total (SW + LW) CRE by tropical cirrus is positive up to a threshold optical thickness of ~3 (reaching a maximum of 29 W m⁻² prior to that point); clouds thicker than that threshold exert a negative CRE. For high cirrus, with cloud top height above 310 hPa, this threshold is larger, ~9. It is also evident from the figure that the magnitude of the total CRE for thick cirrus decreases with cloud top height because of a partial cancellation of SW and LW CREs. It is also noteworthy that the trends shown in Figure 3.15 are likely to vary depending on the temperature difference between the cloud and its underlying surface and on the albedo of the underlying surface (not shown).

Since the last decades, passive radiometric sensors from satellite platforms are widely used, thanks to their global coverage and long data records. Nevertheless, those sensors are not able to resolve thin sub-visible cirrus

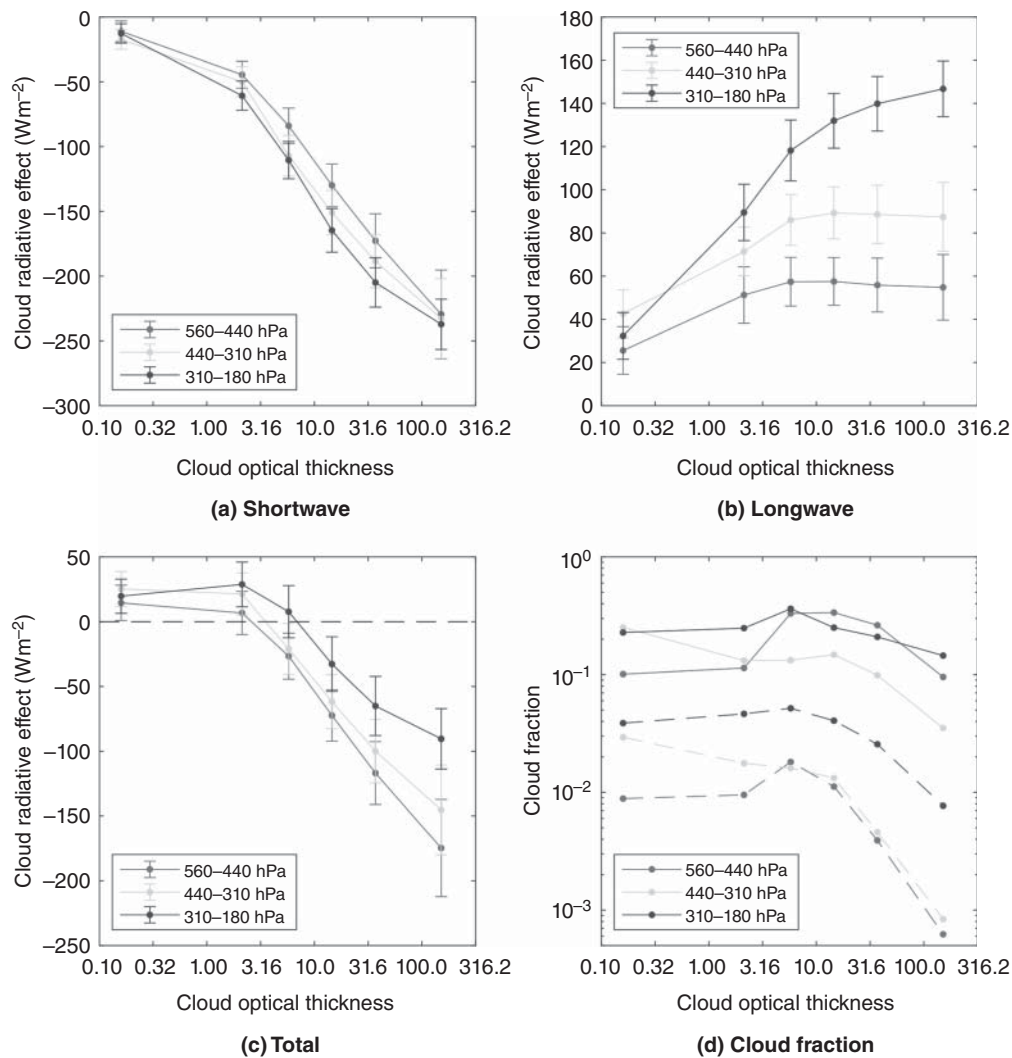


Figure 3.15 Shortwave (a), longwave (b), and total (shortwave + longwave) (c) cloud radiative effect of overcast clouds present over tropics (15°N to 15°S) at the top-of-atmosphere as a function of cloud optical thickness. The cloud top height range is indicated by the legend. Bars represent the standard deviation. Positive values indicate warming (i.e., downward positive). Panel (b) shows cloud fraction derived from MODIS. Solid and dashed lines are maximum and mean cloud fractions of monthly $1^{\circ} \times 1^{\circ}$ gridded values. Cloud properties are derived from daytime observations from MODIS on Terra and Aqua taken from July 2002 through June 2005. Cloud radiative effects are derived from observations by CERES on Terra and Aqua using Edition 4A FluxByCloudTpe. Source: Adapted from Sun et al. (2022).

clouds with an optical depth lower than 0.3, as shown by a recent study (McHardy et al., 2021). On the other hand, the lidar technology shows a higher spatial and temporal resolution, topped with a unique spectral sensitivity. For this reason, lidar is a well-suited instrument for atmospheric profiling the optical, microphysical, and geometrical properties of translucent ice clouds as cirrus. Differently from the passive sensors, the ground-based lidars provide only punctual measurements. Furthermore, the lidar technology shows some issues in detecting cirrus clouds, as shown in Thorsen et al. (2013). In some degree,

the discrepancies in cirrus cloud detection between active and passive remote sensing techniques can be due to the fact that lidar and passive sensors detect different sets of clouds. Cirrus CRE at TOA can be computed through equation (3.12), using the lidar-retrieved vertical profile of the cirrus cloud extinction coefficient as input in the radiative transfer model. Details on single-wavelength lidar equation inversion and its relative uncertainty can be found in Lolli, Di Girolamo, et al. (2017) and Lolli (2021). Other variables needed for the inversion, for example, the molecular extinction and backscattering coefficients, can

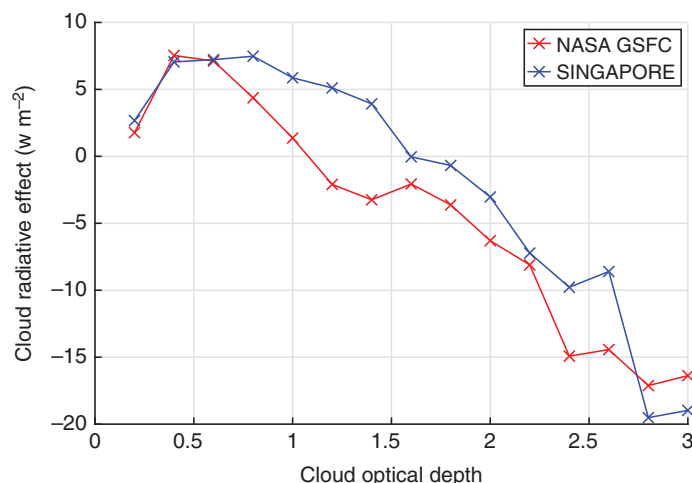


Figure 3.16 Instantaneous daytime net CRE of cirrus clouds as a function of cloud optical depth at Singapore and at NASA GSFC over 1 year of lidar data observations (2010 NASA GSFC and 2012 Singapore).

be obtained using ancillary data and theory, while for the cloud coefficients an assumption is needed to solve the lidar equation (Campbell et al., 2016).

A multi-year analysis of cirrus cloud CRE has been carried out for two ground-based lidar stations, permanent sites of the NASA Micropulse Lidar Network (MPLNET, Welton et al. (2001)). Figure 3.16 shows instantaneous daytime CRE as function of the optical depth from ground-based lidar observations at Singapore and at NASA Goddard Space Flight Center (GSFC). The instantaneous daytime CRE show similar trends with the diurnally averaged CRE values obtained from space-borne observations shown in Figure 3.15. It is interesting to highlight that for equatorial latitudes, there is a shift of the maximum CRE to higher cloud optical thickness with respect to midlatitudes (0.75 for Singapore, 0.45 for GSFC). During daytime, cirrus clouds are warming agents up to an optical depth of 1.6 in the tropics, versus

1.1 in midlatitudes. Overall, daytime clouds at the equator are more warming agents of the Earth-atmosphere system with respect to midlatitude clouds. This is clearly visible in Fig. 3.16, where the Singapore curve has overall higher values than the NASA GSFC curve. Partly, this difference can be explained by the differences in the solar zenith angle and surface temperatures.

3.5.2. Uncertainty in Cirrus CRE Estimations Caused by Crystal Complexity

The influence of ice crystal complexity on the global cirrus CRE has been investigated in studies of Yi et al. (2013) and Järvinen et al. (2018a). Yi et al. (2013) replaced the standard bulk optical properties (β_m , SSA, g) in the Community Atmosphere Model (CAM5.1) with those calculated using smooth and severely roughened ice crystals, assuming a mixture of various habits (Baum et al., 2011). Figure 3.17 shows the difference in the bulk optical

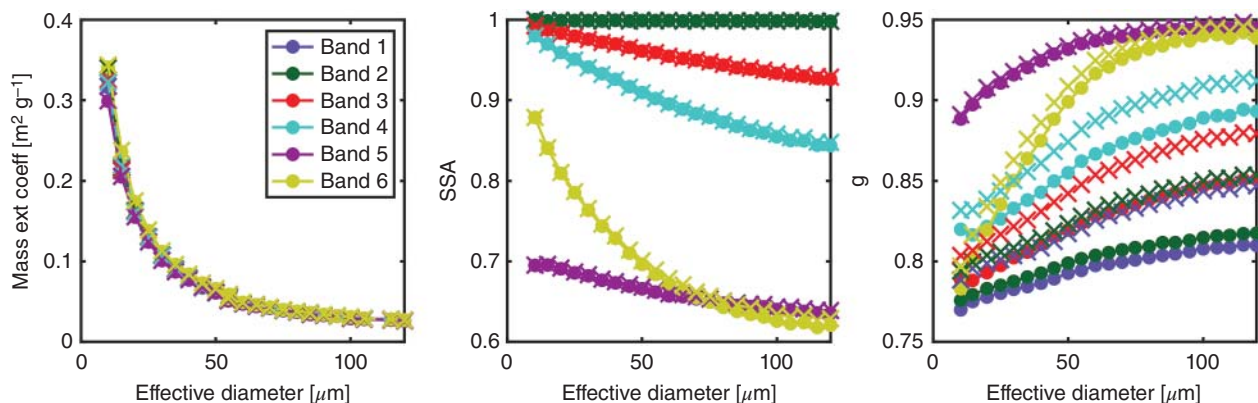


Figure 3.17 The bulk optical properties β_m , SSA, and g as a function of effective diameter for different SW bands for severely roughened crystals (dotted lines) and smooth crystals (crosses). Source: Adapted from Yi et al. (2013).

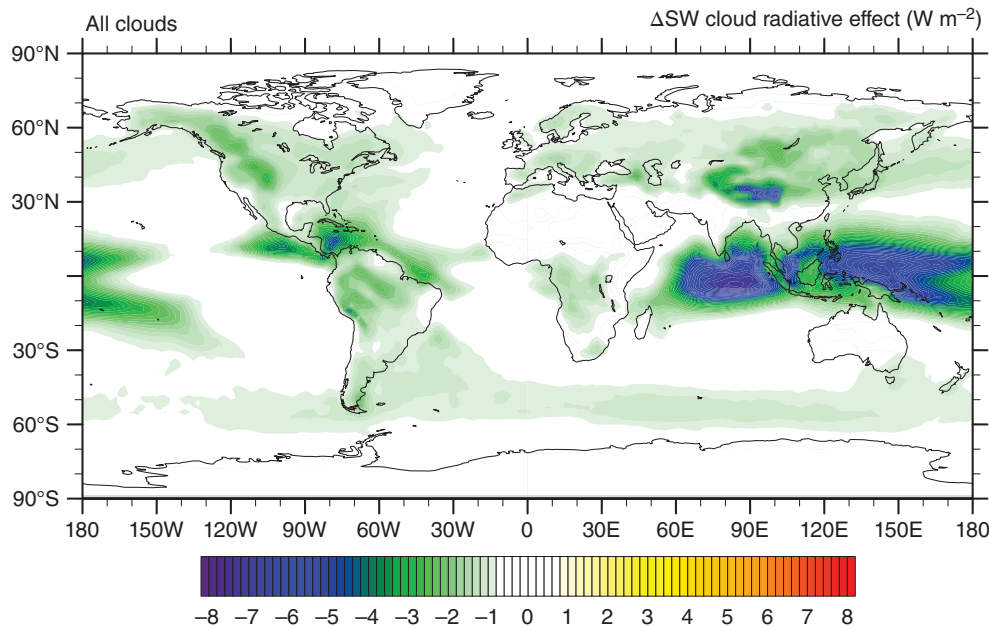


Figure 3.18 Difference in the global SW CRE after changing the current parameterization of g in the ECHAM-HAM model through a new parameterization calculated using severely roughened column aggregates (Yang et al., 2013). The severely roughened column aggregate model was found to best represent in situ measurement of ice cloud angular scattering function. Note that the difference is always negative or zero. Source: Järvinen et al., 2018a / European Geosciences Union / CC BY 4.0.

properties due to addition of facet roughness (using TF method). The primary effect of crystal complexity is seen in the decrease of g in the SW, whereas β_m and SSA are insensitive to crystal complexity. The largest difference in g is seen in the first four SW bands from 0.2 to 0.7 μm . When implementing the results in a radiative transfer model, Yi et al. (2013) found a significant global mean radiative effect of complexity (defined as the difference between simulations using smooth and severely roughened models) of -1.46 W m^{-2} . The net effect was mostly affected by the difference in the SW (-1.83 W m^{-2}), whereas the LW difference was more insignificant (0.37 W m^{-2}). Note that g of severely roughened crystals used in this study for solar wavelengths (band 1) was still substantially higher than the value of 0.75 generally matching observations, which might lead to an underestimation of the effects of crystal complexity on the radiative effect. In addition, Yi et al. (2017) implemented the severely roughened column aggregate model in the RRTMG RTM, which shows good agreement with CERES observation on CRE.

A similar investigation was performed by Järvinen et al. (2018a) who replaced the current parameterization for the bulk g in the ECHAM-HAM global climate model with a parameterization based on severely roughened column aggregate model (Yang et al., 2013). The ice crystal optical model was chosen since it was found to best reproduce in

situ observations of ice cloud angular scattering function at 532 nm. The resulting global mean SW CRE change due to crystal complexity was found to be -1.12 W m^{-2} but a regional change up to -8 W m^{-2} was observed over the Indonesian maritime continent (Fig. 3.18).

Although the effect of crystal complexity on ice cloud (SW) CRE is smaller than the global mean cirrus CRE of about 5 W m^{-2} (Gasparini & Lohmann, 2016; Hong et al., 2016), it is large enough to cause noticeable uncertainty in estimations of the cirrus CRE. For climate model simulations, biases in radiative properties of ice clouds may lead to biases in modeled physical properties of clouds, such as cloud fraction, rain rates, thermodynamic phase, or of other components, such as water vapor profiles. This is because model parameters are generally calibrated (“tuned”) within their uncertainty ranges so that the modeled present-day global radiative fluxes agree with observations and the models are generally energetically balanced in the pre-industrial era (Hourdin et al., 2017; Schmidt et al., 2017; Qian et al., 2018). Given the many parameters included in cloud microphysical schemes and their large uncertainties, such cloud variables are generally targeted as tuning parameters (Hourdin et al., 2017). Hence, relatively small but systematic biases in radiative properties of ice clouds caused by an unrealistic treatment of crystal complexity may have significant impacts on climate models’ skill in representing current atmospheric

variables, and in further predicting changes in climate by increasing greenhouse gasses.

3.6. CONCLUSIONS

The level of detail in natural ice crystals is only just starting to be unraveled. Improved measurement capabilities have made it possible to examine ice crystal structure in the micrometer and sub-micron level. Information on ice crystal complexity has been gained from laboratory and from atmospheric measurements using in situ and polarimetric remote sensing techniques. These observations have led to a consensus that most natural ice crystals deviate from pristine hexagonal geometry.

In this chapter, we have used the term “crystal complexity” to describe all possible deviations from that of a pristine hexagonal prism. Such crystal complexities are identified in a wide scale from nanometer-scale facet roughness to microscale phenomena, such as aggregation. CSEM studies and airborne cloud particle imaging probes have indicated that some degree of facet roughness, hollowness, air bubbles, and aerosol inclusions are more a rule than an exception. Frequently, several types of complexities are observed in the same crystal population or even combined in a single crystal.

Crystal complexity can contain a random component, such as random facet roughening, or it can have a non-random form that mimics the typical sixfold symmetry of the ice crystal, as is the case typically with hollowing. There is no uniform way to quantify morphological complexity but different (physical) complexity parameters are applied depending on the observational method used. To describe the optical effect of ice crystal complexity, a frequently used method in atmospheric sciences is the “tilted facet” method, where the normal of the crystal facet surface is tilted randomly from its nominal orientation during ray-tracing calculations. Other, more realistic, methods are also applied but these require more computational resources and, thus, are only applicable for smaller crystal sizes. Crossover between physical and optical complexity parameters is not yet established, although CSEM studies have shown that the statistical distribution of the square of the surface gradient of laboratory-grown ice can often be well described with gradient distributions assumed in the TF method, such as Gaussian and Weibull.

Cirrus ice crystals are influenced by a variety of environmental conditions during their life cycle, such as supersaturation, subsaturation, or they can interact with other particles in collisions. All these conditions affect the crystal morphology and degree of complexity. Laboratory studies with artificially generated ice crystals have indicated that physical complexity parameters tend to increase with increasing crystal growth rate. In cloud

chamber studies, complexity parameters have been found to linearly correlate with the available condensable water vapor – defined by growth temperature and ice saturation ratio. Sublimation of ice crystals can either result in a rounding of the crystal’s edges, as seen in cloud particle imaging probes, or yield random facet roughness and an increase in the degree of crystal complexity, as seen in laboratory studies. Laboratory studies have also shown that repeated growth and sublimation cycles can lead to a memory effect and gradual buildup of complexity.

Remote sensing and in situ measurements in natural cirrus have not been able to show a clear link between complexity parameters and simultaneously measured temperature or RH_{ice} . This may be due to the fact that the history of individual ice crystals cannot be quantified from crystal formation to point of measurement, and that such history likely contains multiple growth and sublimation cycles that cannot be easily mimicked in laboratory conditions. However, observations of multi-angle solar reflectances and polarimetry have shown that complexity parameters only weakly vary with cloud top temperatures below 230 K. Partly, this observation can be attributed to the fact that remote sensing techniques yield the maximum allowed complexity parameter for most observations, which also suggests that the optical complexity parameterizations probably do not adequately represent the full range of crystal complexity in natural ice clouds. In situ observations have also shown a weak variation in complexity parameters between 230 K and 210 K but a significant increase at temperatures colder than 210 K. Remote sensing and in situ measurements also indicate an increase of complexity in subsaturated conditions. Furthermore, both remote sensing and in situ measurements have shown that complexity parameters increase with increasing ice crystal effective radius, consistent with laboratory observations that have shown that a faster growth rate of large crystals leads to a higher degree of complexity. However, faster growth rates cannot explain the increase of complexity parameter at the coldest temperatures below 210 K, where ice crystals are expected to grow slower and reach smaller sizes. In turn, a slower growth rate also means it takes longer for a crystal to grow to a considerable size, potentially exposing it to a wider range of conditions, including subsaturated conditions, which promotes complexity.

The morphologies of ice crystals largely affect their single-scattering properties in the SW. Since there is no analytical solution to describe the interaction of electromagnetic radiation with aspherical ice crystals, numerical approximations are needed. In case of ice crystals, geometric ray-tracing is usually used to calculate light ray refractions and reflections. Additionally, diffraction needs to be accounted for. To account for crystal complexity,

a random procedure is generally used for determining the outgoing direction of a traced ray in the ray-tracing process.

Calculated ice crystal optical properties are needed for remote sensing retrievals and for radiative transfer calculations. For radiative transfer, three ice crystal single-scattering properties are important: the extinction cross-section, SSA, and angular scattering function (or asymmetry parameter), of which the latter is highly sensitive to crystal complexity. Theoretical and laboratory studies as well as field observations have shown that complex crystals have a smooth and featureless angular scattering function with increased scattering intensity in the angular range from 100° to 150° , which leads to a decrease in the asymmetry parameter. Remote sensing and in situ observations indicate that at temperatures typical of cirrus cloud (below 235 K) a relatively stable asymmetry parameter below 0.79 in the visible represents most global ice clouds, although substantial variation is seen in individual cases that may depend on temperature, humidity, cloud type, and other factors. For ice clouds with cloud tops warmer than 240 K, remote sensing observations have shown an increase in g with increasing cloud top temperature. However, a limitation of space-borne remote sensing measurements is that g can be only retrieved for ice crystals within the first few optical depths from the cloud top.

Cirrus and ice cloud CRE is driven by cloud optical thickness. In general, optically thin cirrus is considered to have a net warming effect while optically thicker (in tropics optical thickness >3) cirrus is considered to have a net cooling effect. The global mean cirrus CRE is considered to be around 5 W m^{-2} . Crystal complexity creates a source of uncertainty in the estimations of ice cloud CRE for a given cloud optical thickness and height through its influence on the magnitude of SW g . Model studies implementing optical parameterizations of complex crystals have shown that taking into account crystal complexity makes ice clouds with a given optical thickness more reflective, with an estimated effect on global SW CRE between 1 and 2 W m^{-2} .

3.7. RECOMMENDATIONS FOR FUTURE WORK

In order to increase the fundamental understanding of crystal complexity, it is recommended that a complexity parameterization crossover should be aimed for. For example, CSEM work provides the most detailed information about the morphology of crystal complexity, but cannot be easily applied to atmospheric ice crystals, whereas in situ measured complexity parameters, such as k_e , cannot be used to discriminate between different complexity types. Thus, a crossover between k_e and CSEM observations is needed. Such crossover can be achieved,

for example, by implementing measurement of spatial light scattering patterns in CSEM.

The same recommendations can be made for physical complexity parameters and optical complexity models. Whereas the TF method has established itself as a popular way to model the optical effects of ice crystal complexity, it hardly provides a good representation of the actual physical facet roughness, nor does it represent the vast scale of other types of complexities observed in cirrus ice crystals. More realistic facet roughness models incorporating the surface slope distributions observed by CSEM should be incorporated into optical particle models. Also, more work should go toward investigating the sensitivity of ice crystal single-scattering properties to different types and degrees of complexity.

Recent developments in ice microphysical schemes for cloud and climate models (e.g., Jensen et al., 2017; Zhang et al., 2014) are able to predict the evolution of ice particle shape and density as crystals are subjected to varying atmospheric conditions. Such schemes could be extended to include complexity metrics, for example, by using empirical relationships derived from in situ and laboratory measurements, while results could be constrained by in situ and remote sensing observations. Additional work is also needed to understand ice crystal growth and sublimation cycles in small-scale models with domains up to few cubic meters.

In general, our knowledge of crystal complexity and its magnitude in natural clouds is still very limited. Remote sensing observations presented here were restricted to optically thicker clouds (optical thickness >5) and to measurements of cloud tops, whereas in situ observations of complexity parameters (e.g., with the SID-3 instrument) have been rare. Open questions remain, such as if the conclusions presented for optically thicker clouds can be applied for optically thinner cirrus, or what is the vertical structure of crystal complexity. On the scale of individual ice crystals, not enough is known on the origin of crystal complexity and how the complexity correlates with other microphysical properties, such as habit, or with crystal formation mechanisms (heterogeneous or homogeneous nucleation, liquid-origin, or in situ origin). Therefore, it is recommended to implement in situ measurements of crystal complexity and ice crystal optical properties as part of the standard flight instrumentation payloads.

Direct measurements of ice crystal optical properties are important for improving radiative transfer calculations. We have shown that calculating g theoretically only based on crystal size or shape can lead to very different g values than are seen in natural clouds. Furthermore, airborne single particle measurement methods in atmospheric sciences have, for decades, focused on discrete detection of light scattering signals by measuring typically one and in some cases up to three signals.

Although detection of one signal is adequate to retrieve particle size, pseudo-continuous 2-D (e.g., SID-3) light scattering patterns are needed for more detailed information on the crystal morphology. Such experimental systems are already applied in other fields (Romanov & Yurkin, 2021) and they should also be more frequently incorporated into atmospheric measurement applications (both in laboratory and field studies).

The results presented in this chapter indicate that ice crystal complexity is relevant for ice cloud radiative properties. Ignoring the optical effects of crystal complexity can lead to systematic biases in radiative properties of ice clouds, and hence to biases in modeled physical cloud properties. Therefore, it is recommended to develop ice microphysical schemes to predict the variation of ice crystal complexity and combine these with flexible ice optical properties schemes to provide consistent radiative properties.

ACKNOWLEDGMENTS

WebPlotDigitizer was used to extract datapoints for Figure 3.17. Emma Järvinen acknowledges funding through the Helmholtz Association's Initiative and Networking Fund (grant agreement no. VH-NG-1531). Bastiaan van Dienenhoven acknowledges funding by NASA through grants no. 80NSSC20M0224 (PACE-SAT) and NNX14AJ28G (TASNPP). Steven Neshyba acknowledges support from NSF, grant CHE-1807898. Martin Schnaiter acknowledges support from the Helmholtz Association research program "Atmosphere and Climate" and funding from the German Research Foundation (grants SCHN 1140/3-1 and SCHN 1140/3-2). Fritz Waitz acknowledges funding by the German Research Foundation (DFG grant JA 2818/1-1).

REFERENCES

- Abdelmonem, A., Järvinen, E., Duft, D., Hirst, E., Vogt, S., Leisner, T., & Schnaiter, M. (2016). PHIPS-HALO: The airborne particle habit imaging and polar scattering probe – Part 1: Design and operation'. *Atmospheric Measurement Techniques*, 9(7), 3131–3144.
- Avila, E. E., Castellano, N. E., Saunders, C. P. R., Bürgesser, R. E., & Aguirre Varela, G. G. (2009). Initial stages of the riming process on ice crystals. *Geophysical Research Letters*, 36(9).
- Bacon, N. J., & Swanson, B. D. (2000). Laboratory measurements of light scattering by single levitated ice crystals. *Journal of the Atmospheric Sciences*, 57(13), 2094–2104.
- Bailey, M., & Hallett, J. (2002). Nucleation effects on the habit of vapour grown ice crystals from -18 to -42°C. *Quarterly Journal of the Royal Meteorological Society: A Journal of the Atmospheric Sciences, Applied Meteorology and Physical Oceanography*, 128(583), 1461–1483.
- Bailey, M., & Hallett, J. (2004). Growth rates and habits of ice crystals between -20 and -70°C. *Journal of the Atmospheric Sciences*, 61(5), 514–544.
- Bailey, M. P., & Hallett, J. (2009). A comprehensive habit diagram for atmospheric ice crystals: Confirmation from the laboratory. AIRS II, and other field studies. *Journal of the Atmospheric Sciences*, 66(9), 2888–2899.
- Baran, A. J. (2009). A review of the light scattering properties of cirrus. *Journal of Quantitative Spectroscopy and Radiative Transfer*, 110(14), 1239–1260. XI Conference on Electromagnetic and Light Scattering by Non-Spherical Particles: 2008.
- Baran, A. J. (2012). From the single-scattering properties of ice crystals to climate prediction: A way forward. *Atmospheric Research*, 112, 45–69.
- Barkey, B., Paulson, S., & Liou, K.-N. (2012). Polar nephelometers for light scattering by ice crystals and aerosols: Design and measurements. In *Light scattering reviews* (Vol. 6, pp. 3–37). Springer.
- Baum, B. A., Yang, P., Heymsfield, A. J., Schmitt, C. G., Xie, Y., Bansemir, A., et al. (2011). Improvements in shortwave bulk scattering and absorption models for the remote sensing of ice clouds. *Journal of Applied Meteorology and Climatology*, 50(5), 1037–1056.
- Bi, L., & Yang, P. (2017). Improved ice particle optical property simulations in the ultraviolet to far-infrared regime. *Journal of Quantitative Spectroscopy and Radiative Transfer*, 189, 228–237.
- Bi, L., Yang, P., Kattawar, G. W., & Mishchenko, M. I. (2013). Efficient implementation of the invariant imbedding T-matrix method and the separation of variables method applied to large nonspherical inhomogeneous particles. *Journal of Quantitative Spectroscopy and Radiative Transfer*, 116, 169–183.
- Bi, L., Yang, P., Liu, C., Yi, B., Baum, B., Van Dienenhoven, B., & Iwabuchi, H. (2014). Assessment of the accuracy of the conventional ray-tracing technique: Implications in remote sensing and radiative transfer involving ice clouds. *Journal of Quantitative Spectroscopy and Radiative Transfer*, 146, 158–174.
- Borovoi, A., Konoshonkin, A., & Kustova, N. (2014). Backscatter ratios for arbitrary oriented hexagonal ice crystals of cirrus clouds. *Optics Letters*, 39(19), 5788.
- Borovoi, A., Kustova, N., & Konoshonkin, A. (2015). Interference phenomena at backscattering by ice crystals of cirrus clouds. *Optics Express*, 23(19), 24557.
- Boucher, O., Randall, D., Artaxo, P., Bretherton, C., Feingold, G., Forster, P., et al. (2013). Clouds and aerosols. In *Climate change 2013: The physical science basis. Contribution of Working Group I to the Fifth Assessment Report of the Intergovernmental Panel on Climate Change* (pp. 571–657). Cambridge University Press.
- Butterfield, N., Rowe, P. M., Stewart, E., Roesel, D., & Neshyba, S. P. (2017). Quantitative three-dimensional ice roughness from scanning electron microscopy. *Journal of Geophysical Research (Atmospheres)*, 122(5), 3023–3041.
- Campbell, J., Lolli, S., Lewis, J., Gu, Y., & Welton, E. (2016). Daytime cirrus cloud top-of-the-atmosphere radiative forcing properties at a midlatitude site and their global consequences. *Journal of Applied Meteorology and Climatology*, 55(8), 1667–1679.

- Campbell, J. R., Dolinar, E. K., Lolli, S., Fochesatto, G. J., Gu, Y., Lewis, J. R., et al. (2021). Cirrus cloud top-of-the-atmosphere net daytime forcing in the Alaskan Subarctic from ground-based MPLNET monitoring. *Journal of Applied Meteorology and Climatology*, 60(1), 51–63.
- Chauvigné, A., Jourdan, O., Schwarzenboeck, A., Gourbeyre, C., Gayet, J. F., Voigt, C., et al. (2018). Statistical analysis of contrail to cirrus evolution during the contrail and cirrus experiment (concert). *Atmospheric Chemistry and Physics*, 18(13), 9803–9822.
- Chepfer, H., Goloub, P., Riedi, J., De Haan, J., Hovenier, J., & Flamant, P. (2001). Ice crystal shapes in cirrus clouds derived from POLDER/ADEOS-1. *Journal of Geophysical Research: Atmospheres*, 106, 7955–7966.
- Cole, B. H., Yang, P., Baum, B. A., Riedi, J., & C-Labonnote, L. (2014). Ice particle habit and surface roughness derived from PARASOL polarization measurements. *Atmospheric Chemistry and Physics*, 14(7), 3739–3750.
- Collier, C. T., Hesse, E., Taylor, L., Ulanowski, Z., Penttilä, A., & Nousiainen, T. (2016). Effects of surface roughness with two scales on light scattering by hexagonal ice crystals large compared to the wavelength: DDA results. *Journal of Quantitative Spectroscopy and Radiative Transfer*, 182, 225–239.
- Connolly, P., Saunders, C., Gallagher, M., Bower, K., Flynn, M., Choularton, T., et al. (2005). Aircraft observations of the influence of electric fields on the aggregation of ice crystals. *Quarterly Journal of the Royal Meteorological Society: A Journal of the Atmospheric Sciences, Applied Meteorology and Physical Oceanography*, 131(608), 1695–1712.
- Cox, C., & Munk, W. (1954). Measurement of the roughness of the sea surface from photographs of the sun's glitter. *Journal of the Optical Society of America* 44(11), 838–850.
- del Genio, A. D., Yao, M.-S., Kovari, W., & Lo, K. K. W. (1996). A prognostic cloud water parameterization for global climate models. *Journal of Climate*, 9(2), 270–304.
- Draine, B. T., & Flatau, P. J. (1994). Discrete-dipole approximation for scattering calculations. *JoSAA*, 11(4), 1491–1499.
- Dugin, V., Volkovitskii, O., Mirumians, S., & Nikiforova, N. (1977). Anisotropy of light scattering by artificial crystalline cloud formations. *Academy of Sciences, USSR, Izvestiya, Atmospheric and Oceanic Physics*, 13, 22–25.
- Forster, L., Seefeldner, M., Baumgartner, A., Kölling, T., & Mayer, B. (2020). Ice crystal characterization in cirrus clouds II: Radiometric characterization of HaloCam for the quantitative analysis of halo displays. *Atmospheric Measurement Techniques*, 13(7), 3977–3991.
- Freudenthaler, V., Homburg, F., & Jäger, H. (1996). Optical parameters of contrails from lidar measurements: Linear depolarization. *Geophysical Research Letters*, 23(25), 3715–3718.
- Fridlind, A., Atlas, R., Van Diedenhoven, B., Um, J., McFarquhar, G., Ackerman, A., et al. (2016). Derivation of physical and optical properties of mid-latitude cirrus ice crystals for a size-resolved cloud microphysics model. *Atmospheric Chemistry and Physics*, 16(11), 7251–7283.
- Garrett, T. J., Gerber, H., Baumgardner, D. G., Twohy, C. H., & Weinstock, E. M. (2003). Small, highly reflective ice crystals in low-latitude cirrus. *Geophysical Research Letters*, 30(21).
- Garrett, T. J., Hobbs, P. V., & Gerber, H. (2001). Shortwave, single-scattering properties of Arctic ice clouds. *Journal of Geophysical Research: Atmospheres*, 106(D14), 15155–15172.
- Gasparini, B., Blossey, P. N., Hartmann, D. L., Lin, G., & Fan, J. (2019). What drives the life cycle of tropical anvil clouds?. *Journal of Advances in Modeling Earth Systems*, 11, 2586–2605.
- Gasparini, B., & Lohmann, U. (2016). Why cirrus cloud seeding cannot substantially cool the planet. *Journal of Geophysical Research: Atmospheres*, 121(9), 4877–4893.
- Gayet, J.-F., Auriol, F., Oshchepkov, S., Schröder, F., Duroure, C., Febvre, G. et al. (1998). In situ measurements of the scattering phase function of stratocumulus, contrails and cirrus. *Geophysical Research Letters*, 25(7), 971–974.
- Gayet, J.-F., Ovarlez, J., Shcherbakov, V., Ström, J., Schumann, U., Minikin, A. et al. (2004). Cirrus cloud microphysical and optical properties at southern and northern midlatitudes during the inca experiment. *Journal of Geophysical Research: Atmospheres*, 109(D20).
- Gayet, J.-F., Shcherbakov, V., Voigt, C., Schumann, U., Schäuble, D., Jessberger, P., et al. (2012). The evolution of microphysical and optical properties of an A380 contrail in the vortex phase. *Atmospheric Chemistry and Physics*, 12(14), 6629–6643.
- Geogdzhayev, I., & van Diedenhoven, B. (2016). The effect of roughness model on scattering properties of ice crystals. *Journal of Quantitative Spectroscopy and Radiative Transfer*, 178, 134–141.
- Gerber, H., Takano, Y., Garrett, T. J., & Hobbs, P. V. (2000). Nephelometer measurements of the asymmetry parameter, volume extinction coefficient, and backscatter ratio in Arctic clouds. *Journal of the Atmospheric Sciences*, 57(18), 3021–3034.
- Gultepe, I., Heymsfield, A. J., Gallagher, M., Ickes, L., & Baumgardner, D. (2017). Ice fog: The current state of knowledge and future challenges. *Meteorological Monographs*, 58, 4–1.
- Hallett, J., & Mossop, S. C. (1974). Production of secondary ice particles during the riming process. *Nature*, 249(5452), 26–28.
- Hartmann, D. L., Gasparini, B., Berry, S. E., & Blossey, P. N. (2018). The life cycle and net radiative effect of tropical anvil clouds. *Journal of Advances in Modeling Earth Systems*, 10, 3012–3029.
- Hesse, E., Macke, A., Havemann, S., Baran, A., Ulanowski, Z., & Kaye, P. H. (2012). Modelling diffraction by faceted particles. *Journal of Quantitative Spectroscopy and Radiative Transfer*, 113(5), 342–347.
- Heymsfield, A. J., Krämer, M., Luebke, A., Brown, P., Cziczo, D. J., Franklin, C., et al. (2017). Cirrus clouds. *Meteorological Monographs*, 58, 2–1.
- Hioki, S., Yang, P., Baum, B. A., Platnick, S., Meyer, K. G., King, M. D., & Riedi, J. (2016). Degree of ice particle surface roughness inferred from polarimetric observations. *Atmospheric Chemistry and Physics*, 16(12), 7545–7558.
- Holz, R. E., Platnick, S., Meyer, K., Vaughan, M., Heidinger, A., Yang, P., et al. (2016). Resolving ice cloud optical thickness biases between CALIOP and MODIS using infrared retrievals. *Atmospheric Chemistry and Physics*, 16(8), 5075–5090.

- Hong, G., & Minnis, P. (2015). Effects of spherical inclusions on scattering properties of small ice cloud particles. *Journal of Geophysical Research: Atmospheres*, 120(7), 2951–2969.
- Hong, G., Yang, P., Baum, B. A., Heymsfield, A. J., & Xu, K.-M. (2009). Parameterization of shortwave and longwave radiative properties of ice clouds for use in climate models. *Journal of Climate*, 22(23), 6287–6312.
- Hong, Y., Liu, G., & Li, J.-L. F. (2016). Assessing the radiative effects of global ice clouds based on CloudSat and CALIPSO measurements. *Journal of Climate*, 29(21), 7651–7674.
- Hourdin, F., Mauritsen, T., Gettelman, A., Golaz, J.-C., Balaji, V., Duan, Q., et al. (2017). The Art and Science of Climate Model Tuning. *Bulletin of the American Meteorological Society*, 98(3), 589–602.
- Huffman, P. (1970). Polarization of light scattered by ice crystals. *Journal of the Atmospheric Sciences*, 27(8), 1207–1208.
- Järvinen, E., Jourdan, O., Neubauer, D., Yao, B., Liu, C., Andreae, M. O. et al. (2018a). Additional global climate cooling by clouds due to ice crystal complexity. *Atmospheric Chemistry and Physics*, 18(21), 15767–15781.
- Jensen, A. A., Harrington, J. Y., Morrison, H., & Milbrandt, J. A. (2017). Predicting ice shape evolution in a bulk microphysics model. *Journal of the Atmospheric Sciences*, 74(6), 2081–2104.
- Johnson, B. R. (1988). Invariant imbedding T-matrix approach to electromagnetic scattering. *Applied Optics*, 27(23), 4861–4873.
- Jourdan, O., Oshchepkov, S., Shcherbakov, V., Gayet, J.-F., & Isaka, H. (2003). Assessment of cloud optical parameters in the solar region: Retrievals from airborne measurements of scattering phase functions. *Journal of Geophysical Research: Atmospheres*, 108(D18).
- Järvinen, E., Schnaiter, M., Mioche, G., Jourdan, O., Shcherbakov, V. N., Costa, A. et al. (2016). Quasi-spherical ice in convective clouds. *Journal of the Atmospheric Sciences*, 73(10), 3885–3910.
- Järvinen, E., Wernli, H., & Schnaiter, M. (2018b). Investigations of mesoscopic complexity of small ice crystals in midlatitude cirrus. *Geophysical Research Letters*, 45(20), 11,465–11,472.
- Kahnert, M., Nousiainen, T., Thomas, M. A., & Tynnelä, J. (2012). Light scattering by particles with small-scale surface roughness: Comparison of four classes of model geometries. *Journal of Quantitative Spectroscopy and Radiative Transfer*, 113(18), 2356–2367.
- Kato, S., Loeb, N. G., Rutan, D. A., & Rose, F. G. (2020). Effects of electromagnetic wave interference on observations of the Earth radiation budget. *Journal of Quantitative Spectroscopy and Radiative Transfer*, 253, 107157.
- Kato, S., Rose, F. G., Rutan, D. A., & Charlock, T. P. (2008). Cloud effects on the meridional atmospheric energy budget estimated from Clouds and the Earth's Radiant Energy System (CERES) data. *Journal of Climate*, 21, 4223–4241.
- Krämer, M., Rolf, C., Spelten, N., Afchine, A., Fahey, D., Jensen, E. et al. (2020). A microphysics guide to cirrus – Part 2: Climatologies of clouds and humidity from observations. *Atmospheric Chemistry and Physics*, 20(21), 12569–12608.
- Laubert, A., Kiselev, A., Pander, T., Handmann, P., & Leisner, T. (2018). Secondary ice formation during freezing of levitated droplets. *Journal of the Atmospheric Sciences*, 75, 2815–2826.
- Lawson, R. P., Woods, S., Jensen, E., Erfani, E., Gurganus, C., Gallagher, M. et al. (2019). A review of ice particle shapes in cirrus formed in situ and in anvils. *Journal of Geophysical Research: Atmospheres*, 124(17–18), 10049–10090.
- Letu, H., Ishimoto, H., Riedi, J., Nakajima, T. Y., -Labonnote, L. C., Baran, A. J., Nagao, T. M., et al. (2016). Investigation of ice particle habits to be used for ice cloud remote sensing for the GCOM-C satellite mission. *Atmospheric Chemistry & Physics*, 16(18), 12287–12303.
- Liou, K.-N., & Yang, P. (2016). *Light scattering by ice crystals: Fundamentals and applications*. Cambridge University Press.
- Liu, C., Lee Panetta, R., & Yang, P. (2013). The effects of surface roughness on the scattering properties of hexagonal columns with sizes from the Rayleigh to the geometric optics regimes. *Journal of Quantitative Spectroscopy and Radiative Transfer*, 129, 169–185.
- Liu, C., Panetta, R. L., & Yang, P. (2012). Application of the pseudo-spectral time domain method to compute particle single-scattering properties for size parameters up to 200. *Journal of Quantitative Spectroscopy and Radiative Transfer*, 113(13), 1728–1740.
- Liu, C., Yang, P., Minnis, P., Loeb, N., Kato, S., Heymsfield, A., & Schmitt, C. (2014). A two-habit model for the microphysical and optical properties of ice clouds. *Atmospheric Chemistry and Physics*, 14, 13719–13737.
- Liu, Q. H. (1997). The PSTD algorithm: A time-domain method requiring only two cells per wavelength. *Microwave and Optical Technology Letters*, 15(3), 158–165.
- Loeb, N. G., Kato, S., Loukachine, K., & Smith, N. M. (2005). Angular distribution models for top-of-atmosphere radiative flux estimation from the Clouds and the Earth's Radiant Energy System instrument on the Terra satellite. Part I: Methodology. *Journal of Atmospheric and Oceanic Technology*, 22, 338–351.
- Loeb, N. G., Yang, P., Rose, F. G., Hong, G., Sun-Mack, S., Minnis, P., et al. (2018). Impact of ice cloud microphysics on satellite cloud retrievals and broadband flux radiative transfer model calculations. *Journal of Climate*, 31, 1851–1864.
- Lolli, S. (2021). Is the air too polluted for outdoor activities? check by using your photovoltaic system as an air-quality monitoring device. *Sensors (Basel, Switzerland)*, 21(19).
- Lolli, S., Campbell, J., Lewis, J., Gu, Y., Marquis, J., Chew, B., et al. (2017). Daytime top-of-the-atmosphere cirrus cloud radiative forcing properties at Singapore. *Journal of Applied Meteorology and Climatology*, 56(5), 1249–1257.
- Lolli, S., Di Girolamo, P., Demoz, B., Li, X., & Welton, E. (2017). Rain evaporation rate estimates from dual-wavelength lidar measurements and intercomparison against a model analytical solution. *Journal of Atmospheric and Oceanic Technology*, 34(4), 829–839.
- Lu, R.-S., Tian, G.-Y., Gledhill, D., & Ward, S. (2006). Grinding surface roughness measurement based on the co-occurrence matrix of speckle pattern texture. *Applied Optics*, 45(35), 8839–8847.
- L'Ecuyer, T. S., Wood, N. B., Haladay, T., Stephens, G. L., & Stackhouse, Jr., P. W. (2008). Impact of clouds on atmospheric heating based on the R04 CloudSat flux and heating rate data set. *Journal of Geophysical Research: Atmospheres*, 113.

- Mace, G. G., Zhang, Q., Vaughan, M., Marchand, R., Stephens, G., Trepte, C., & Winker, D. (2009). A description of hydrometeor layer occurrence statistics derived from the first year of merged CloudSat and CALIPSO data. *Journal of Geophysical Research: Atmospheres*, 114(D8).
- Macke, A., Francis, P. N., McFarquhar, G. M., & Kinne, S. (1998). The role of ice particle shapes and size distributions in the single scattering properties of cirrus clouds. *Journal of the Atmospheric Sciences*, 55(17), 2874–2883.
- Macke, A., Mishchenko, M. I., & Cairns, B. (1996). The influence of inclusions on light scattering by large ice particles. *Journal of Geophysical Research: Atmospheres*, 101(D18), 23311–23316.
- Macke, A., Mueller, J., & Raschke, E. (1996). Single scattering properties of atmospheric ice crystals. *Journal of the Atmospheric Sciences*, 53(19), 2813–2825.
- Maeno, N. (1967). Air bubble formation in ice crystals. *Physics of Snow and Ice: Proceedings*, 1(1), 207–218.
- Magee, N. B., Miller, A., Amaral, M., & Cumiskey, A. (2014). Mesoscopic surface roughness of ice crystals pervasive across a wide range of ice crystal conditions. *Atmospheric Chemistry and Physics*, 14(22), 12357–12371.
- Magee, N., Boaggio, K., Staskiewicz, S., Lynn, A., Zhao, X., Tusay, N. et al. (2020). Captured cirrus ice particles in high definition. *Atmospheric Chemistry and Physics*, 2020, 1–27.
- Magono, C., & Lee, C. W. (1966). Meteorological classification of natural snow crystals. *Journal of the Faculty of Science, Hokkaido University. Series 7, Geophysics*, 2(4), 321–335.
- Matus, A. V., & L'Ecuyer, T. S. (2017). The role of cloud phase in Earth's radiation budget. *Journal of Geophysical Research*, 122(5), 2559–2578.
- McFarquhar, G. M., Yang, P., Macke, A., & Baran, A. J. (2002). A new parameterization of single scattering solar radiative properties for tropical anvils using observed ice crystal size and shape distributions. *Journal of the Atmospheric Sciences*, 59(16), 2458–2478.
- McHardy, T. M., Campbell, J. R., Peterson, D. A., Lolli, S., Bankert, R. L., Garnier, A., et al. (2021). Advancing maritime transparent cirrus detection using the advanced baseline imager “cirrus” band. *Journal of Atmospheric and Oceanic Technology*, 38(6), 1093–1110.
- Min, M., Wang, P., Campbell, J. R., Zong, X., & Li, Y. (2010). Midlatitude cirrus cloud radiative forcing over China. *Journal of Geophysical Research: Atmospheres*, 115(D20).
- Mioche, G., Josset, D., Gayet, J.-F., Pelon, J., Garnier, A., Minikin, A., & Schwarzenboeck, A. (2010). Validation of the CALIPSO-CALIOP extinction coefficients from in situ observations in midlatitude cirrus clouds during the CIRCLE-2 experiment. *Journal of Geophysical Research: Atmospheres*, 115(D4).
- Mishchenko, M. I., & Macke, A. (1998). Incorporation of physical optics effects and computation of the Legendre expansion for ray-tracing phase functions involving δ -function transmission. *Journal of Geophysical Research: Atmospheres*, 103(D2), 1799–1805.
- Mishchenko, M. I., & Sassen, K. (1998). Depolarization of lidar returns by small ice crystals: An application to contrails. *Geophysical Research Letters*, 25(3), 309–312.
- Mishchenko, M. I., & Travis, L. D. (1998). Capabilities and limitations of a current FORTRAN implementation of the T-matrix method for randomly oriented, rotationally symmetric scatterers. *Journal of Quantitative Spectroscopy and Radiative Transfer*, 60(3), 309–324.
- Mishchenko, M., Rossow, W., Macke, A., & Lacis, A. (1995). Effect of particle nonsphericity on bidirectional reflectance of cirrus clouds. In *Proceedings of the 1995 ARM Science Meeting* (pp. 19–23). San Diego, CA, March.
- Morrison, H., & Gettelman, A. (2008). A new two-moment bulk stratiform cloud microphysics scheme in the Community Atmosphere Model, Version 3 (CAM3). Part I: Description and numerical tests. *Journal of Climate*, 21(15), 3642–3659.
- Mosimann, L., Steiner, M., Collett, J., Henrich, W., Schmid, W., & Waldvogel, A. (1993). Ice crystal observations and the degree of riming in winter precipitation. *Water Air Soil Pollution*, 68, 29–42.
- Murray, B. J., Salzmann, C. G., Heymsfield, A. J., Dobbie, S., Neely, III, R. R., Cox, C. J., et al. (2015). Trigonal ice crystals in Earth's atmosphere. *Bulletin of the American Meteorological Society*, 96(9), 1519–1531.
- Nelson, J., & Swanson, B. D. (2019). Lateral facet growth of ice and snow—part 1: Observations and applications to secondary habits. *Atmospheric Chemistry and Physics*, 19(24), 15285–15320.
- Neshyba, S. P., Lowen, B., Benning, M., Lawson, A., & Rowe, P. M. (2013). Roughness metrics of prismatic facets of ice. *Journal of Geophysical Research (Atmospheres)*, 118(8), 3309–3318.
- Nousiainen, T., & McFarquhar, G. M. (2004). Light scattering by quasi-spherical ice crystals. *Journal of the Atmospheric Sciences*, 61(18), 2229–2248.
- Nousiainen, T., & Muinonen, K. (2007). Surface-roughness effects on single-scattering properties of wavelength-scale particles. *Journal of Quantitative Spectroscopy and Radiative Transfer*, 106(1–3), 389–397.
- Okamoto, H., Sato, K., Borovoi, A., Ishimoto, H., Masuda, K., Konoshonkin, A., & Kustova, N. (2020). Wavelength dependence of ice cloud backscatter properties for space-borne polarization lidar applications. *Optics Express*, 28(20), 29178.
- Ono, A. (1969). The shape and riming properties of ice crystals in natural clouds. *Journal of Atmospheric Sciences*, 26(1), 138–147.
- Pfalzgraff, W. C., Hulscher, R. M., & Neshyba, S. P. (2010). Scanning electron microscopy and molecular dynamics of surfaces of growing and ablating hexagonal ice crystals. *Atmospheric Chemistry and Physics*, 10(6), 2927–2935.
- Pfisterer, R. N. (2011). Approximated scatter models for stray light analysis. *Optics and Photonics News*, 22(10), 16–17.
- Purcell, E. M., & Pennypacker, C. R. (1973). Scattering and absorption of light by nonspherical dielectric grains. *The Astrophysical Journal*, 186, 705–714.
- Qian, Y., Wan, H., Yang, B., Golaz, J. C., Harrop, B., Hou, Z., et al. (2018). Parametric sensitivity and uncertainty quantification in the version 1 of E3SM Atmosphere Model based on short Perturbed Parameter Ensemble Simulations. *Journal of Geophysical Research: Atmospheres*, 123(23), 13,046–13,073.
- Ramanathan, V., Cess, R. D., Harrison, E. F., Minnis, P., Barkstrom, B. R., Ahmad, E., & Hartmann, D. (1989).

- Cloud-radiative forcing and climate: Results from the Earth Radiation Budget Experiment. *Science*, 243, 57–63.
- Rimmer, J., & Saunders, C. (1997). Radiative scattering by artificially produced clouds of hexagonal plate ice crystals. *Atmospheric Research*, 45(2), 153–164.
- Riskilä, E., Lindqvist, H., & Muinonen, K. (2021). Light scattering by fractal roughness elements on ice crystal surfaces. *Journal of Quantitative Spectroscopy and Radiative Transfer*, 267, 107561.
- Romanov, A. V., & Yurkin, M. A. (2021). Single-particle characterization by elastic light scattering. *Laser and Photonics Reviews*, 2000368, 1–18.
- Saito, M., Yang, P., Heidinger, A. K., & Li, Y. (2020). An improved beta method for ice cloud property retrievals: Theory. *Journal of Geophysical Research (Atmospheres)*, 125(14), e31863.
- Sasaki, Y., Nishiyama, N., & Furukawa, Y. (1998). Experimental study on light scattering from an artificial ice cloud. *Polar Meteorology and Glaciology*, 12, 130–139.
- Sassen, K., Kayetha, V. K., & Zhu, J. (2012). Ice cloud depolarization for nadir and off-nadir CALIPSO measurements. *Geophysical Research Letters*, 39(20).
- Sassen, K., & Liou, K.-N. (1979). Scattering of polarized laser light by water droplet, mixed-phase and ice crystal clouds. Part I: Angular scattering patterns. *Journal of the Atmospheric Sciences*, 36(5), 838–851.
- Sassen, K., Wang, Z., & Liu, D. (2008). Global distribution of cirrus clouds from Cloudsat/Cloud-Aerosol Lidar and Infrared Pathfinder Satellite Observations (CALIPSO) measurements. *Journal of Geophysical Research: Atmospheres* 113(D8).
- Sassen, K., & Zhu, J. (2009). A global survey of CALIPSO linear depolarization ratios in ice clouds: Initial findings. *Journal of Geophysical Research: Atmospheres*, 114(D4).
- Schmidt, G. A., Bader, D., Donner, L. J., Elsaesser, G. S., Golaz, J.-C., Hannay, C. et al. (2017). Practice and philosophy of climate model tuning across six US modeling centers. *Geoscientific Model Development*, 10(9), 3207–3223.
- Schmitt, C. G., & Heymsfield, A. J. (2007). On the occurrence of hollow bullet rosette- and column-shaped ice crystals in mid-latitude cirrus. *Journal of the Atmospheric Sciences*, 64(12), 4514–4519.
- Schmitt, C. G., & Heymsfield, A. J. (2014). Observational quantification of the separation of simple and complex atmospheric ice particles. *Geophysical Research Letters*, 41(4), 1301–1307.
- Schmitt, C. G., Heymsfield, A. J., Connolly, P., Järvinen, E., & Schnaiter, M. (2016). A global view of atmospheric ice particle complexity. *Geophysical Research Letters*, 43(22), 11,913–11,920.
- Schmitt, C. G., Stuefer, M., Heymsfield, A. J., & Kim, C. K. (2013). The microphysical properties of ice fog measured in urban environments of Interior Alaska. *Journal of Geophysical Research Atmospheres*, 118(19), 11136–11147.
- Schnaiter, M., Büttner, S., Möhler, O., Skrotzki, J., Vragel, M., & Wagner, R. (2012). Influence of particle size and shape on the backscattering linear depolarisation ratio of small ice crystals—cloud chamber measurements in the context of contrail and cirrus microphysics. *Atmospheric Chemistry and Physics*, 12(21), 10465–10484.
- Schnaiter, M., Järvinen, E., Abdelmonem, A., & Leisner, T. (2018). PHIPS_HALO: The airborne particle habit imaging and polar scattering probe – Part 2: Characterization and first results. *Atmospheric Measurement Techniques*, 11(1), 341–357.
- Schnaiter, M., Järvinen, E., Vochezer, P., Abdelmonem, A., Wagner, R., Jourdan, O. et al. (2016). Cloud chamber experiments on the origin of ice crystal complexity in cirrus clouds. *Atmospheric Chemistry and Physics*, 16(8), 5091–5110.
- Shcherbakov, V., Gayet, J.-F., Jourdan, O., Minikin, A., Ström, J., & Petzold, A. (2005). Assessment of cirrus cloud optical and microphysical data reliability by applying statistical procedures. *Journal of Atmospheric and Oceanic Technology*, 22(4), 409–420.
- Shcherbakov, V., Gayet, J.-F., Jourdan, O., Ström, J., & Minikin, A. (2006). Light scattering by single ice crystals of cirrus clouds. *Geophysical Research Letters*, 33(15), L15809.
- Soden, B. J., Broccoli, A. J., & Hemler, R. S. (2004). On the use of cloud forcing to estimate cloud feedback. *Journal of Climate*, 17, 3661–3665.
- Sohn, B. J., Nakajima, T., Satoh, M., & Jang, H.-S. (2010). Impact of different definitions of clear-sky flux on the determination of longwave cloud radiative forcing: NICAM simulation results. *Atmospheric Chemistry and Physics*, 10, 11641–11646.
- Stephens, G. L., Gabriel, P. M., & Partain, P. T. (2001). Parameterization of atmospheric radiative transfer. Part I: Validity of simple models. *Journal of the Atmospheric Sciences*, 58(22), 3391–3409.
- Stephens, G. L., Tsay, S.-C., Stackhouse, Paul W., J., & Flatau, P. J. (1990). The relevance of the microphysical and radiative properties of cirrus clouds to climate and climatic feedback. *Journal of the Atmospheric Sciences*, 47(14), 1742–1754.
- Stoelinga, M. T., Locatelli, J. D., Woods, C. P., Stoelinga, M. T., Locatelli, J. D., & Woods, C. P. (2007). The occurrence of “irregular” ice particles in stratiform clouds. *Journal of the Atmospheric Sciences*, 64(7), 2740–2750.
- Su, W., Corbett, J., Eitzen, Z., & Liang, L. (2015). Next-generation angular distribution models for top-of-atmosphere radiative flux calculation from CERES instruments: Validation. *Atmospheric Measurement Techniques*, 8.
- Sun, M., Doelling, D. R., Loeb, N. G., Scott, R. C., Wilkins, J., Nguyen, L. T., & Mlynarczyk, P. (2022). Clouds and the Earth’s Radiant Energy System (CERES) FluxByCIdTyp edition 4 data product. *Journal of Atmospheric and Oceanic Technology*, 39(3), 303–318.
- Sun, W., Fu, Q., & Chen, Z. (1999). Finite-difference time-domain solution of light scattering by dielectric particles with a perfectly matched layer absorbing boundary condition. *Applied Optics*, 38(15), 3141–3151.
- Taflove, A., & Umashankar, K. R. (1990). The finite-difference time-domain method for numerical modeling of electromagnetic wave interactions. *Electromagnetics*, 10(1–2), 105–126.
- Takahashi, T. (1993). High ice crystal production in winter cumuli over the Japan Sea. *Geophysical Research Letters*, 20(6), 451–454.
- Takano, Y., & Liou, K. (1995). Radiative transfer in cirrus clouds. Part III: Light scattering by irregular ice crystals. *Journal of Atmospheric Sciences*, 52(7), 818–837.

- Takano, Y., Liou, K., & Minnis, P. (1992). The effects of small ice crystals on cirrus infrared radiative properties. *Journal of Atmospheric Sciences*, 49(16), 1487–1493.
- Tang, G., Panetta, R. L., Yang, P., Kattawar, G. W., & Zhai, P.-W. (2017). Effects of ice crystal surface roughness and air bubble inclusions on cirrus cloud radiative properties from remote sensing perspective. *Journal of Quantitative Spectroscopy and Radiative Transfer*, 195, 119–131. Laser-light and Interactions with Particles 2016.
- Tape, W., & Moilanen, J. (2006). Atmospheric Halos and the search for Angle X. (Vol. 58). Washington, D. C: American Geophysical Union.
- Thorsen, T. J., Fu, Q., & Comstock, J. M. (2013). Cloud effects on radiative heating rate profiles over darwin using arm and A-Train radar/lidar observations. *Journal of Geophysical Research: Atmospheres*, 118(11), 5637–5654.
- Twomey, S. (1977). *Atmospheric aerosols*. Elsevier Scientific publishing Co.
- Ulanowski, Z., Hesse, E., Kaye, P. H., & Baran, A. J. (2006). Light scattering by complex ice-analogue crystals. *Journal of Quantitative Spectroscopy and Radiative Transfer*, 100(1), 382–392. VIII Conference on Electromagnetic and Light Scattering by Nonspherical Particles.
- Ulanowski, Z., Kaye, P. H., Hirst, E., Greenaway, R. S., Cotton, R. J., Hesse, E., & Collier, C. T. (2014). Incidence of rough and irregular atmospheric ice particles from Small Ice Detector 3 measurements. *Atmospheric Chemistry and Physics*, 14(3), 1649–1662.
- Um, J., & McFarquhar, G. M. (2007). Single-scattering properties of aggregates of bullet rosettes in cirrus. *Journal of Applied Meteorology and Climatology*, 46(6), 757.
- Um, J., & McFarquhar, G. M. (2011). Dependence of the single-scattering properties of small ice crystals on idealized shape models. *Atmospheric Chemistry and Physics*, 11(7), 3159–3171.
- Um, J., McFarquhar, G. M., Hong, Y. P., Lee, S.-S., Jung, C. H., Lawson, R. P., & Mo, Q. (2015). Dimensions and aspect ratios of natural ice crystals. *Atmospheric Chemistry and Physics*, 15(7), 3933–3956.
- van Diedenhoven, B. (2014). The prevalence of the 22° halo in cirrus clouds. *Journal of Quantitative Spectroscopy and Radiative Transfer*, 146, 475–479.
- van Diedenhoven, B. (2018). Remote sensing of crystal shapes in ice clouds, In: Kokhanovsky, A. (eds) *Springer Series in Light Scattering*. Springer Series in Light Scattering. Springer, Cham.
- van Diedenhoven, B. (2021). Variation of ice microphysical properties with temperature and humidity at tops of convective clouds. *Geophysical Research Letters*, 48(16), e2021GL093673.
- van Diedenhoven, B., Ackerman, A. S., Fridlind, A. M., Cairns, B., & Riedi, J. (2020). Global statistics of ice microphysical and optical properties at tops of optically thick ice clouds. *Journal of Geophysical Research (Atmospheres)*, 125(6), e31811.
- van Diedenhoven, B., Cairns, B., Geogdzhayev, I. V., Fridlind, A. M., Ackerman, A. S., Yang, P., & Baum, B. A. (2012). Remote sensing of ice crystal asymmetry parameter using multi-directional polarization measurements - Part 1: Methodology and evaluation with simulated measurements. *Atmospheric Measurement Techniques*, 5, 2361–2374.
- van Diedenhoven, B., Fridlind, A. M., Ackerman, A. S., & Cairns, B. (2012). Evaluation of hydrometeor phase and ice properties in cloud-resolving model simulations of tropical deep convection using radiance and polarization measurements. *Journal of Atmospheric Sciences*, 69(11), 3290–3314.
- Vogelmann, A. M., & Ackerman, T. P. (1995). Relating cirrus cloud properties to observed fluxes: A critical assessment. *Journal of the Atmospheric Sciences*, 52(23), 4285–4301.
- Voigtländer, J., Chou, C., Bieligk, H., Clauss, T., Hartmann, S., Herenz, P. et al. (2018). Surface roughness during depositional growth and sublimation of ice crystals. *Atmospheric Chemistry and Physics*, 18(18), 13687–13702.
- Walden, V. P., Warren, S. G., & Tuttle, E. (2003). Atmospheric ice crystals over the Antarctic Plateau in winter. *Journal of Applied Meteorology*, 42(10), 1391–1405.
- Wang, Y., Yang, P., Hioki, S., King, M. D., Baum, B. A., Di Girolamo, L., & Fu, D. (2019). Ice cloud optical thickness, effective radius, and ice water path inferred from fused MISR and MODIS measurements based on a pixel-level optimal ice particle roughness model. *Journal of Geophysical Research (Atmospheres)*, 124(22), 12,126–12,140.
- Waterman, P. C. (1971). Symmetry, unitarity, and geometry in electromagnetic scattering, *Physical Review D*, 3(4), 825.
- Welton, E. J., Campbell, J. R., Spinhirne, J. D., & Stanley Scott III, V. (2001). Global monitoring of clouds and aerosols using a network of micropulse lidar systems, *SPIE Asia-Pacific Remote Sensing*.
- Wielicki, B. A., Barkstrom, B. R., Harrison, E. F., Lee, R. B., Smith, G. L., & Cooper, J. E. (1996). Clouds and the Earth's Radiant Energy System (CERES): An Earth observing system experiment. *Bulletin of the American Meteorological Society*, 77, 853–868.
- Woods, S., Lawson, R. P., Jensen, E., Bui, T., Thornberry, T., Rollins, A., et al. (2018). Microphysical properties of tropical tropopause layer cirrus. *Journal of Geophysical Research: Atmospheres*, 123(11), 6053–6069.
- Xie, Y., Yang, P., Kattawar, G. W., Minnis, P., & Hu, Y. X. (2009). Effect of the inhomogeneity of ice crystals on retrieving ice cloud optical thickness and effective particle size. *Journal of Geophysical Research: Atmospheres*, 114(D11).
- Xu, G., Schnaiter, M., & Järvinen, E. (2022). Accurate retrieval of asymmetry parameter for large and complex ice crystals from in-situ polar nephelometer measurements. *Journal of Geophysical Research: Atmospheres*, 127(3), e2021JD036071.
- Yang, P., Bi, L., Baum, B. A., Liou, K.-N., Kattawar, G. W., Mishchenko, M. I., & Cole, B. (2013). Spectrally consistent scattering, absorption, and polarization properties of atmospheric ice crystals at wavelengths from 0.2 to 100 μm . *Journal of the Atmospheric Sciences*, 70(1), 330–347.
- Yang, P., Hioki, S., Saito, M., Kuo, C.-P., Baum, B., & Liou, K.-N. (2018). A review of ice cloud optical property models for passive satellite remote sensing. *Atmosphere*, 9(12), 499.
- Yang, P., & Liou, K. (1996a). Finite-difference time domain method for light scattering by small ice crystals in three-dimensional space. *JOSA A*, 13(10), 2072–2085.

- Yang, P., & Liou, K. (1996b). Geometric-optics–integral-equation method for light scattering by nonspherical ice crystals. *Applied Optics*, 35(33), 6568–6584.
- Yang, P., & Liou, K. (1998a). Single-scattering properties of complex ice crystals in terrestrial atmosphere. *Beitrage zur Physik der Atmosphäre-Contributions to Atmospheric Physics*, 71(2), 223–248.
- Yang, P., & Liou, K.-N. (1998b). *Single-scattering properties of complex ice crystals in terrestrial atmosphere*. Germany.
- Yang, P., Zhang, L., Hong, G., Nasiri, S. L., Baum, B. A., Huang, H., et al. (2007). Differences between collection 4 and 5 MODIS ice cloud optical/microphysical products and their impact on radiative forcing simulations. *IEEE Transactions on Geoscience and Remote Sensing*, 45(9), 2886–2899.
- Yi, B., Rapp, A. D., Yang, P., Baum, B. A., & King, M. D. (2017). A comparison of aqua MODIS ice and liquid water cloud physical and optical properties between collection 6 and collection 5.1: Cloud radiative effects. *Journal of Geophysical Research: Atmospheres*, 122(8), 4550–4564.
- Yi, B., Yang, P., Baum, B. A., L'Ecuyer, T., Oreopoulos, L., Mlawer, E. J., et al. (2013). Influence of ice particle surface roughening on the global cloud radiative effect. *Journal of the Atmospheric Sciences*, 70(9), 2794–2807.
- Yorks, J. E., Hlavka, D. L., Hart, W. D., & McGill, M. J. (2011). Statistics of cloud optical properties from airborne lidar measurements. *Journal of Atmospheric and Oceanic Technology*, 28, 869–883.
- Yurkin, M. A., & Hoekstra, A. G. (2011). The discrete-dipole-approximation code ADDA: Capabilities and known limitations. *Journal of Quantitative Spectroscopy and Radiative Transfer*, 112(13), 2234–2247.
- Yurkin, M. A., Hoekstra, A. G., Brock, R. S., & Lu, J. Q. (2007). Systematic comparison of the discrete dipole approximation and the finite difference time domain method for large dielectric scatterers. *Optics Express*, 15(26), 17902–17911.
- Zhang, C., Harrington, J. Y., Zhang, C., & Harrington, J. Y. (2014). Including surface kinetic effects in simple models of ice vapor diffusion. *Journal of the Atmospheric Sciences*, 71(1), 372–390.
- Zhang, M., Teng, S., Di, D., Hu, X., Letu, H., Min, M., & Liu, C. (2020). Information content of ice cloud properties from multi-spectral, -angle and -polarization observations. *Remote Sensing*, 12(16), 2548.
- Zhang, Y., Macke, A., & Albers, F. (1999). Effect of crystal size spectrum and crystal shape on stratiform cirrus radiative forcing. *Atmospheric Research*, 52(1), 59–75.
- Zhao, W., Peng, Y., Wang, B., Yi, B., Lin, Y., & Li, J. (2018). Comparison of three ice cloud optical schemes in climate simulations with community atmospheric model version 5. *Atmospheric Research*, 204(Jan), 37–53.
- Zhao, X., Lin, Y., Peng, Y., Wang, B., Morrison, H., & Gettelman, A. (2017). A single ice approach using varying ice particle properties in global climate model microphysics. *Journal of Advances in Modeling Earth Systems*, 9(5), 2138–2157.